Mechanisms and energetics in the early stages of solvent-assisted low-temperature sintering of ZnO

Lucas Villatte, Maria-Isabel Rua-Taborda, Arnaud Ndayishimiye, Clive Randall, Alain Largeteau, Graziella Goglio, Catherine Elissalde, Sylvie Bordère

▶ To cite this version:

Lucas Villatte, Maria-Isabel Rua-Taborda, Arnaud Ndayishimiye, Clive Randall, Alain Largeteau, et al.. Mechanisms and energetics in the early stages of solvent-assisted low-temperature sintering of ZnO. Materialia, 2022, 22, pp.101417. 10.1016/j.mtla.2022.101418 . hal-03673069

Mechanisms and Energetics in the early stages of solvent-assisted low-temperature sintering of ZnO

Lucas Villatte[a], Maria-Isabel Rua-Taborda[a], Arnaud Ndayishimiye[b, c], Clive A. Randall[b, c], Alain Largeteau[a], Graziella Goglio[a], Catherine Elissalde[a] and Sylvie Bordère[d].

[a] *Univ. Bordeaux, CNRS, Bordeaux INP, ICMCB, UMR 5026, F-33600 Pessac, France*

[b] *Materials Research Institute, The Pennsylvania State University, University Park, PA 16802, United States*

[c] *Department of Materials Science and Engineering, The Pennsylvania State University, University Park, PA 16802, United States*

[d] *CNRS, University of Bordeaux, Arts et Métiers Institute of Technology, Bordeaux INP, INRAE, I2M Bordeaux, F-33400, Talence, France*

Abstract

The Hydro/Solvothermal Sintering (HSS) is a technique enabling the low temperature sintering of ceramics and composites, by using a solvent and uniaxial pressure. This energy-efficient technique also opens new perspectives in designing new composites with tailored functional properties. While the solvent plays a key role in reducing the sintering temperature, the modelling and deep understanding of sintering mechanisms remain an open field of investigation. This study unveils the energetics and mechanisms involved in the first stage of HSS. The strategy highlighted in this paper includes: i) the building of a hydrothermal sintering device equipped with a dilatometer to monitor the shrinkage *in situ*, ii) numerical stress calculations at the contact between particles to show the suitability of the two-particle kinetic equation, and iii) the use of anisothermal and non-conventional stepwise isothermal methodologies for the investigation of mechanisms and energetics. The model material, ZnO, was densified to high relative densities with acetic acid as a solvent, and a pressure and temperature of 320 MPa and 150 °C, respectively. With these experimental conditions, the kinetic analysis obtained from the two methodologies is consistent and implies a dissolution reaction of the material as the rate controlling mechanism with possible coupling to grain boundary sliding. The activation energy of 90 $kJ.mol^{-1}$ is determined with the different analysis methodologies. The interest of the stepwise isothermal methodology in obtaining accurate activation energy is also discussed.

Keywords: hydrothermal sintering, modelling, kinetics analysis, mechanism, stepwise isothermal densification approach, zinc oxide.

1. Introduction

Sintering has always been recognized as a complex process involving different transport mechanisms leading to specific microstructural evolutions [1–4]. The development of sintering methods towards advanced processes involving different driving forces or combinations of driving force (Hot Pressing, Spark Plasma Sintering, Flash sintering, microwave sintering, etc.) all impact densification rates and microstructural development in various ways [5–11]. Predicting densification according to the thermal histories and the processing methods has always been the subject of a considerable number of studies covering a wide variety of materials and various approaches [12–20]. Classical isothermal and non-isothermal densification approaches combined with Master Sintering Curve (MSC) or Constant Rate Heating (CRH) methods are very useful in understanding the kinetic parameters of sintering [21–29]. Very recently, the emergence of solvent-assisted, low temperature sintering methods (sintering temperature below 500 °C) has not only provided a major contribution to the development of new materials and composites but has also raised many unanswered questions about specific densification mechanisms that occur at low temperatures previously never considered within sintering models [30–32].

Among the solvent-assisted low sintering temperature processes, the Hydro / Solvothermal Sintering (HSS) is inspired by geological densification processes [33–37]. A uniaxial pressure is applied to a powder in the presence of solvent under hydrothermal conditions over short periods of time. The main driving force is the intra-grain stress gradients induced by the uniaxial pressure applied, leading to a change of the mechano-chemical equilibrium at the liquid / solid interface. The pressure gradient shifts the chemical potential equilibrium in the liquid phase, enabling the dissolution / precipitation phenomena at solid / liquid interfaces. Both the solvent and the high pressure enhance the diffusion process. An analogy with liquid phase sintering, for which a molten phase at high temperature enhances the diffusion process, can be considered because of a comparable stress field configuration, but it is worth noting that the order of magnitude of stress is significantly different, as well as the transient or permanent nature of the liquid. Closely related, but with important differences, is the Cold Sintering Process (CSP), which operates in an open system unlike the HSS that is in a closed system. With CSP, the driving force for densification relies also on the synergy between the mechano-chemical effects (pressure solution creep) and the chemical effects (solvent/particle surface interactions). The surface reactivity-based mechanisms involved in HSS and CSP enable the low-temperature densification (< 500 °C) and have opened major opportunities towards the processing of nanostructured ceramics and new composites, the co-sintering of ceramics, polymers, and the integration of inorganic materials with different structures. A relevant example to highlight the role of the solvent in terms of transient chemistry was given in a comparative study between CSP and HSS of ZnO [38]. The role of chemistry during a water assisted spark plasma sintering of ZnO was already highlighted in the study of Gonzalez-Julian et al [39]. Zinc oxide is particularly well suited to solvent assisted sintering due to a high surface reactivity, with good affinity with appropriate solvents naturally exhibiting congruent solubility to a significant extent.

One of the specificities of the above-mentioned low-temperature sintering methods is the significant influence of the surface chemistry in the early stages of sintering. Thus, a key objective is to determine transport mechanisms involved, including the type of transport (diffusive, viscous) and the mass transport path. The identification of the rate limiting steps and mechanisms will help to define the nature of the densification processes. Conventional approaches, including MSC and CRH, can help understand the specific mechanisms involved in HSS or CSP sintering. Bang et *al.* were the first to identify the densification kinetics through an anisothermal approach applied to CSP sintering of ZnO [40]. The authors have shown that, compared to conventional sintering, the activation energy of ZnO densification is much smaller for the cold sintering process thanks to low temperatures and the use of a compatible transient chemistry. It is also important to note that that work considered heating rates up to 15 °C.min^{-1}, and considered densification rates in the intermediate stage of sintering. The densification kinetics of conventionally sintered ZnO ceramics is well documented [41,42]. Sintering temperatures higher than 900°C are usually required to reach full densification, and the dominant mechanism controlling both initial and intermediate stages of sintering was attributed to grain boundary diffusion.

Here, we aim to analyze from experimental data the kinetics for the very early stages of the sintering of ZnO under non-conventional HSS conditions. A specific apparatus was designed to follow the compressive displacement in the hydrothermal sintering reactor, as a function of the application of the force and the heating temperature. This bench, thus represents a unique device to follow the macroscopic behavior of ZnO during hydrothermal sintering by *in situ* dilatometry. Two different approaches are used and compared to determine the activation energy of the rate-limiting stage and infer the controlling diffusion paths involved in the sintering of ZnO by HSS. As both kinetic approaches are based on the two-particle model, we also discuss the relevance of its application under specific HSS conditions.

2. Kinetic modelling

The two-particle shrinkage rate model dedicated to pressure-less solid state sintering can be reconsidered under an applied pressure condition and with the presence of solvent within the pore phase (*i.e.* HSS conditions). This simplified kinetic equation can be used for 3D compacts with isotropic conditions. So, the last part will show under which conditions the HSS can be approximated to isostatic-like compression, with the aim of providing a reliable interpretation of the kinetic analysis

2.1. Kinetic law from the two-particle model

Kinetic models of particle contact growth and shrinkage have been largely developed from the two spherical particle model, mostly in the case of conventional solid state sintering [1,21,43,44], involving surface tension induced tensile stress at the external border of the neck. These simplified models lead to correct approximation of the initial sintering stage kinetics, post rearrangement of particles, which is analyzed through contact growth between grains and shrinkage. This stage is considered valid until the impingement of necks between adjacent grains, *i.e.* for a shrinkage ranging from 4% (dense) to 10% (loose), depending on the initial compactness of the powder [1].

More precisely, these kinetic models are based on geometric simplifications relating the contact radius x, the penetration depth of one particle into the other h, the particle radius a remaining constant, and the neck radius *r* that prevails for the pressure at the neck surface (see Figure 1S in the Supplementary Information (SI)). Under these assumptions, the modelling developments [1,21,43,44] partly detailed in the SI have given rise to a simplified and known kinetic equation (Eq 1) describing shrinkage in the first stages of sintering:

$$\varepsilon'(t) = K_0(T)e^{-\frac{Q}{RT}}\,\varepsilon^{1-P} \qquad \textit{Eq 1}$$

where K_0 is a function of the absolute temperature T previously defined by Woolfrey and Bannister [23] in the case of diffusion transport through the relation $K_0(T) = k_0/T$, with k_0 a constant for a given material system (see SI), Q the activation energy of the mass transport, ε the linear shrinkage

$\Delta L/L_0 = h/a$ (L being the lengths of the sample), and P the coefficient, which can be related to the pathway of the material transport [1,21,43,44] (see SI and Figure 1).

2.1.1. Particles subjected to uniaxial compression

When the two particles are uniaxially pressed, the general form of the sintering kinetic equation (Eq 1) was shown not to be affected [43,45]. The only modification concerns the k_0-constant in the K_0-function, which can be rewritten as:

$$K_0(T) = \frac{k_0}{T} = \frac{k_0'}{T}\left(\gamma + \frac{p_A a}{\pi}\right) \qquad \textit{Eq 2}$$

where p_A is the applied pressure and k_0' a constant.

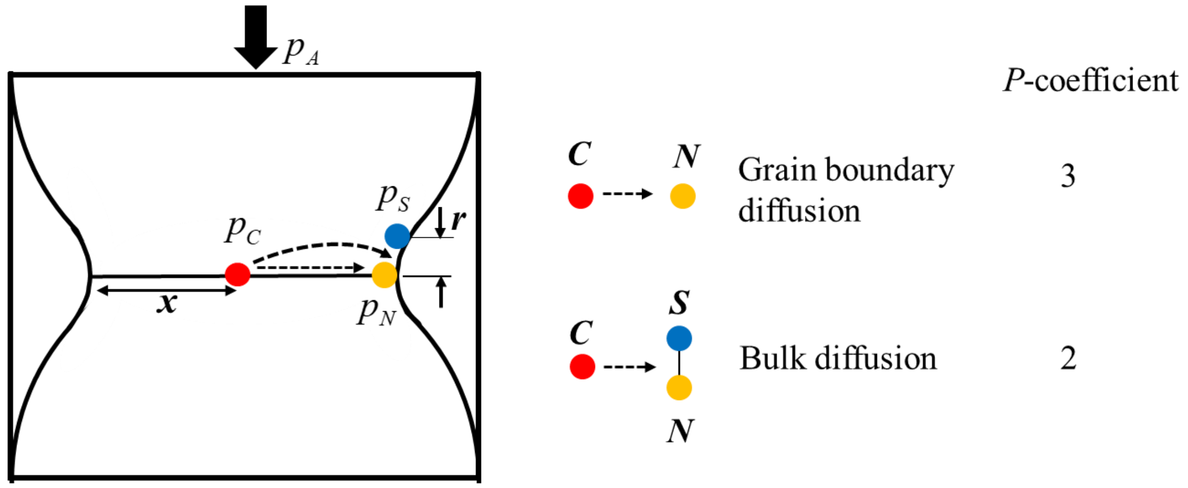

Figure 1 : Diagram showing i) the most likely diffusion pathways taking place (with or without applied pressure) during densifying mechanisms in the solid state sintering, ii) the values of the P-coefficient appearing in Eq 1 and related to the transport mechanism that controls kinetics. During the first stage of densifying process, the characteristic pressures are $p_N - p_\infty = \gamma\left(\frac{1}{R_1}+\frac{1}{R_2}\right) = -\frac{\gamma}{r}+\frac{\gamma}{x} \approx -\frac{\gamma}{r}$*, where* p_∞ *is the pressure of the material under a flat surface* R_1 *and* R_2 *are the algebraic values of the principal curvature radii at point N defined under the sign convention to* $R_1 = -r$ *(curvature center outside the material) and* $R_2 = x$ *(curvature center inside the material); and* $p_C - p_\infty = \frac{p_A a}{\pi r}$.

The term $(\gamma + p_A a/\pi)$ in Eq 2 comes from the pressure gradient in Eq S2 defined in the SI. If this gradient is defined between point C and point N, it gives rise to $\nabla p = \Delta p/x = (p_N - p_C)/x$ (Figure 1), where p_N and p_C are the pressures located at the neck and center of the grain boundary, respectively, for pressure free sintering, $p_N - p_C = (-(\gamma/r) + \gamma/x) \approx -(\gamma/r)$. When the applied pressure as driving force predominates ($p_N - p_\infty \approx 0$) with p_∞ the pressure of the material under a flat surface, this pressure difference is reduced to [45] :

$$\Delta p = p_N - p_C = -\,p_C = -\frac{4p_A a^2}{\pi x^2} = -\frac{p_A a}{\pi r} \qquad \textit{Eq 3}$$

If the two driving forces are of the same order of magnitude, the pressure gradient is thus $\Delta p = -\,1/r\,(\gamma + p_A a/\pi)$, in consistency with the pressure term in the K_0-function (Eq 2).

The relevance of this simple relation (Eq 3) when surface tension is negligible is assessed from the simulation of the stress field induced by a uniaxial pressure p_A applied to the upper limit of the elementary cell of a contact between two grains (Figure 2). The intra-granular pressure map shows a large pressure gradient near the external border of the neck (Figure 2D), with a non-zero value of the pressure p_N in spite of negligible surface tension contributions. Nevertheless, the calculated dimensionless pressure difference $\Delta p/p_A = -18$ (see pressure values in the legend of Figure 2) is very close to the expected model value $\Delta p/p_A = -19$ with $x/a = 0.26$ given by Eq 3. Note that the complete pressure relaxation at the neck is limited by the increase of high shear stress in that area (Figure 2C). From the calculated stress map (Figure 2B and Figure 2D), it is possible to identify the three characteristic points (previously defined in Figure 1) between which the matter can diffuse. These points are reported in Figure 2D. Since $p_C \gg p_N$, mass fluxes from points C to N are thus involved and correspond to the conditions of grain boundary diffusion, the mass transport pathway that is related to the coefficient P = 3 [1,21,43,44] (Figure 1). The pressure value p_S at the point S a distance away ($h = r$) from the contact surface is very close to p_N, thus involving homogeneous fluxes passing through the surface A of the external border of the neck of thickness r. This condition is compatible with bulk diffusion mechanism (see SI) characterized by the coefficient $P = 2$ (Figure 1) [1,21,43,44].

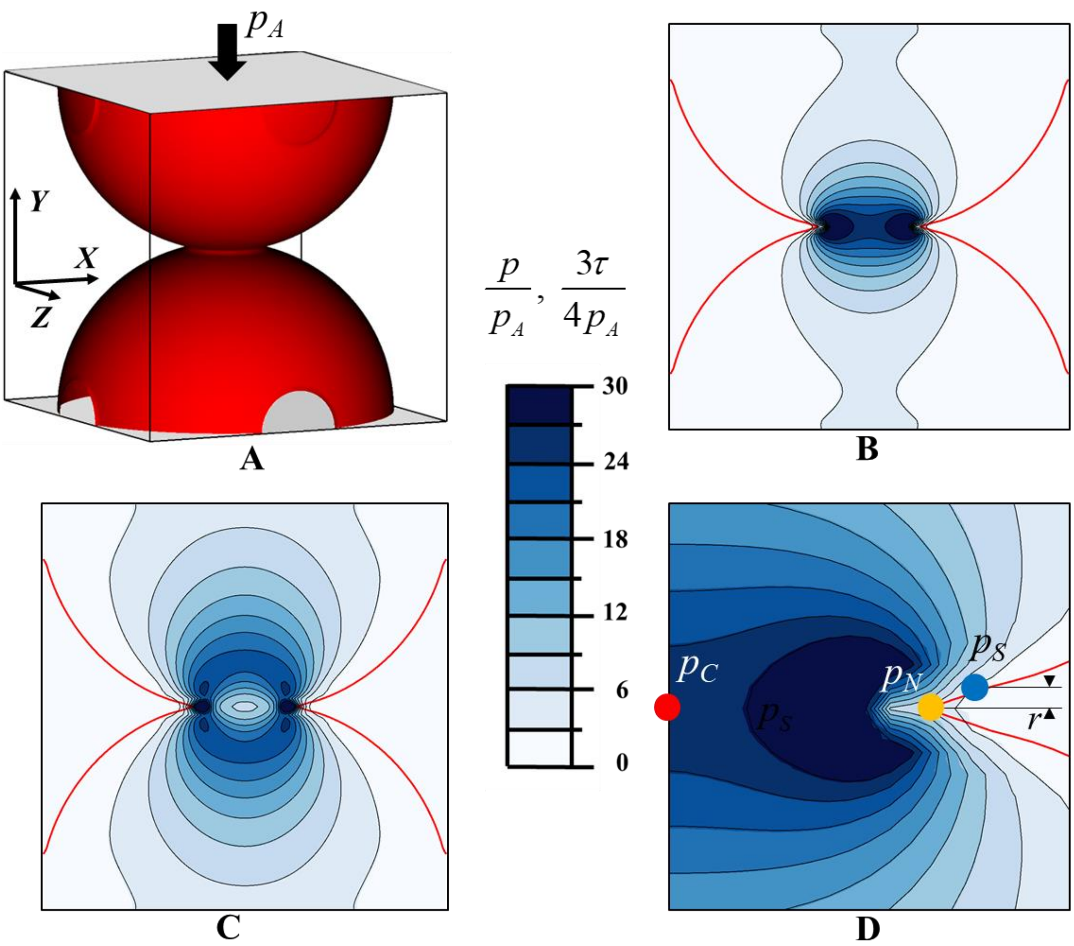

Figure 2 : Maps of hydrostatic (B, D) and shear (C) stresses obtained from the simulation of uniaxial compression applied to the upper boundary of the elementary system representing a contact between two grains (A). Isotropic elasticity is considered with constants defined by the Young's modulus E_Y *= 75 GPa, and Poisson coefficient ν = 0.2. Simulations were performed using the open source code NOTUS [https://notus-cfd.org], based on a volume difference resolution on a fixed grid. Modelling of elastic materials and numerical resolutions are well described in ref [46]. The compression proceeds through a constant velocity applied to the upper limit of the system. The compression is stopped when the mean pressure of this upper surface is* p_A *= 320 MPa. Symmetry boundary conditions are applied to the five other limits. The results are presented using dimensionless variable. The normalized size of the contact radius is* $x/a = 0.26$*. From the pressure maps, the pressure values at the characteristic points are determined:* $p_N/p_A = 7$, $p_C/p_A = 25$, $p_S/p_A = 4$.

2.1.2. Uniaxial pressed particles in the presence of solvent

During hydrothermal sintering, other transport mechanisms can be involved by analogy with geothermal studies-suggested compaction by inter-granular pressure solution of the earth's crust [47–51] involving dissolution / precipitation creep mechanisms.

Indeed, the mechano-chemical equilibrium at the interface solid / solvent leads to a shift of the saturation concentration C of the solute into the solvent depending on the pressure jump $p_{solid} -$

$p_{solvent}$ at the interface [52], by relative to C^* the solute concentration when the pressure in the solid equals the solvent pressure. It can be expressed simply as [53–55]:

$$C = C^* e^{\frac{\Omega(p_{solid} - p_{solvent})}{RT}} \qquad \textit{Eq 4}$$

where Ω is the molar volume of the involved species, which is here considered equal in the solid and in the solvent.

Even if the values of the pressures p_N and p_S are close (Figure 2), a pressure difference exists $(p_N > p_S)$ at the particle surface, implying from Eq 4 a solute concentration difference between point N and S $(C_N - C_S) > 0$. Mass transport from points N to S through the solvent phase is thus induced, which implies the dissolution of the solid at point N and the precipitation of the solute at the external border of the neck between N and S (Figure 3).

Since an atomic-scale layer of water is present on the surface of the particles during the overall HSS process, the presence of the reactive solvent in between the two particles is also considered (Figure 3). In the very early stage of sintering, the high pressure does squeeze out the excess solvent at particle contacts, and the solvent film thickness should be very thin, as suggested in [56]. It can be considered rather as a thin layer of chemisorbed solvent molecules. Based on the assumption that the material dissolved along this supposed adsorbed solvent layer is characterized by its own pressure p_L $(p_{solvent} = p_L)$, higher solute concentrations at point C than at point N are expected through Eq 4. Such dissolution / diffusion / precipitation sequential process was kinetically modelled in the case of liquid phase sintering using the same development steps and geometrical assumptions described in the SI and giving rise to Eq 1 for shrinkage rate modelling [2,18,44,56]. In the case where the kinetics of this sequential process are controlled by the dissolution reaction, the P-coefficient modeled by Kingery [2] and others [56] was equal to 2. In the case where it is diffusion along the solvent layer that controls the kinetics, the P-coefficient obtained was equal to 3 [2,56], in agreement with the grain boundary diffusion involved in the solid state sintering. Note that reverse fluxes of adsorbed solvent species could also diffuse from points N to C, thanks to the large solvent reservoir in the pore space, enhancing solute transport and favoring the film to remain between the two particles. The coefficient P relative to Eq 1 has not yet been defined either in the case where the limiting mechanism is precipitation or diffusion of the solutes from the neck into the liquid phase of the pore space.

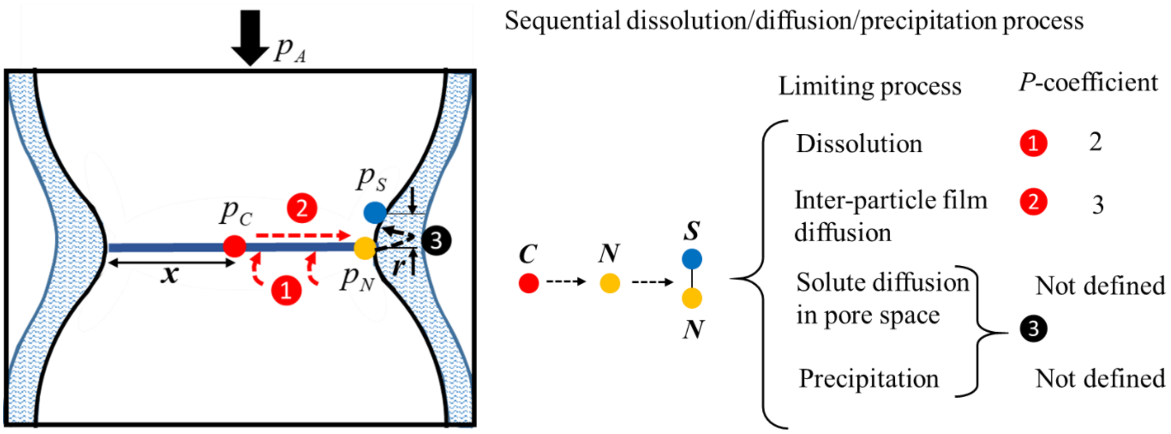

Figure 3 : Diagram showing: i) the most likely diffusion pathways and pressure solution reactions (dissolution and precipitation) involved during the hydrothermal sintering, ii) the values of the P-coefficient appearing in Eq 1 and related to the mechanism that controls the sintering kinetics. ❶ *dissolution in the inter-particle film,* ❷ *diffusion of the solute through the film,* ❸ *dissolution at the external neck border/diffusion in the pore space/precipitation. The geometrical variables involved in the two-particle shrinkage modelling are defined in Figure S1. The characteristic pressures are defined in Figure 1 and Figure 2.*

2.2. Application of the two-particle kinetic law to the 3D compacts

Another important complication is the pressure distribution within the die for both HSS and CSP, namely the uniaxial and radial stresses. The externally applied average forces are indeed in balance with two opposing forces, the transmitted force and the frictional force. The overall frictional forces are associated with both a die wall friction and interparticle frictional forces [57]. Numerous articles show that the radial force in a die is proportional to the applied uniaxial force, and the constant is known as the radial force constant [58].

A detailed 3D representation of multiple particle contacts inside a die is beyond the scope of the present discussion. However, when considering HSS, some physical insights are required in order to verify if the transmission of the applied pressure p_A at the contact between two particles (section

2.1.1) is uniform within the real compact or not, assuming only elastic deformation of particles. The simulation of the two particles compression has already provided some insights since the symmetry boundary conditions are considered at the limits of the system (Figure 2). It means that each hemisphere of the system is in contact with another one in the X and Z directions (Figure 2A). The pressure map within the particles (Figure 2B) shows that the applied pressure p_A is not widely transmitted at the contacts that are parallel to the direction of the load. This explains why the system was equivalent to two particles in contacts (section 2.1.2). So, for compacts for which the particle position is fixed, the applied pressure is transmitted anisotropically, depending on the orientation of the contact. The 2D sintering scenario shown in Figure 4 illustrates the way to obtain an isotropic transmission of the applied pressure to contacts considering frictionless particles rearrangement all along the sintering process. Starting from an isostatic pressing of an elementary two-particle system (Figure 4A), a contact growth gives rise to the shrinkage along the perpendicular loading direction. leading to an anisotropic distribution of the applied pressure in the three directions (Figure 4B). Isotropic pressing can then be recovered again through particle rearrangement involving grain sliding phenomena (Figure 4C-Figure 4D). Note, that this sliding mechanism is facilitated considering the assumption of an adsorbed solvent layer between particles (see section 2.1.2) being expected to increase mass transport at the contact compared to solid state sintering and even at low temperature. This assumption of particle contact growth and shrinkage during hydrothermal sintering, which is intermingled with particle sliding mechanism, has also been pointed out in the case of SPS sintering, which also involving uniaxial loading [12,59,60]

The statistical mean calculation of the contact pressure p_C for iso-pressed random packing has been studied and defined [61] as:

$$p_C = \frac{4p_A a^2}{Zx^2} = \frac{p_A a}{Zr} \qquad \text{Eq 5}$$

where Z is the average coordination number of the particles. A similar equation has been proposed with an additional dependence of this pressure with powder density D [62,63]. It becomes:

$$p_C = \frac{4p_A a^2}{ZDx^2} = \frac{p_A a}{ZDr} \qquad \textit{Eq 6}$$

So, these definitions of contact pressure for an isostatic pressing of a particle compact highlight that the function K_0 is not only dependent on the temperature variable, as it was shown for the two-particle model Eq 2, but could also be dependent on the coordination number Z (Eq 5), which can vary during sintering, and possibly depends also on the powder packing density D (Eq 6).

So, in considering all the above, the use of the kinetic Eq 1 to characterize the first stage of hydrothermal sintering is relevant if the particles sliding is easy enough to induce isostatic pressing leading to homogeneous contact pressure. Note that this pressure contact induced by isotropic pressing was also considered earlier for SPS kinetic equations [12,64]. Considering the contact pressure of Eq 6, the function K_0 can be defined for the compact as:

$$K_0(T, Z, D) = \frac{k_0'}{T}\left(\gamma + \frac{p_A a}{ZD}\right) \qquad \textit{Eq 7}$$

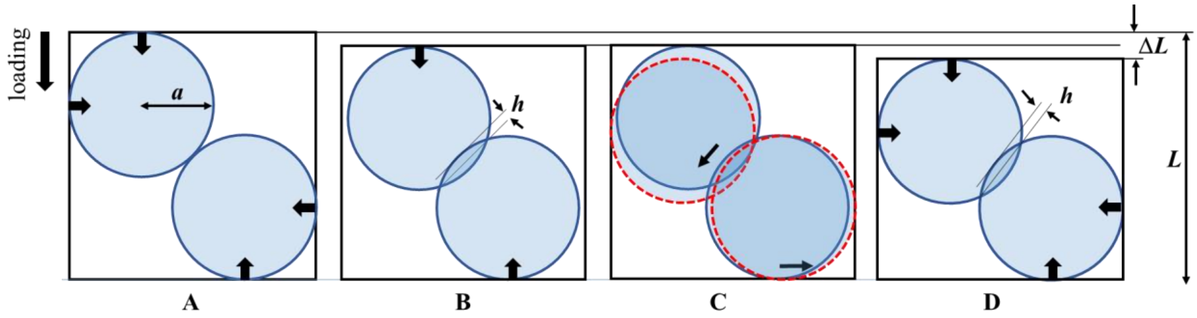

Figure 4 : 2D sintering scenario illustrating the grain sliding mechanism associated with local particle shrinkage and that allows to recover an isostatic pressing. A: local two-particle contact with isostatic pressing; B: two-particle shrinkage; C: sliding mechanism for particle rearrangement; D: recovery of isostatic pressing.

3. Methodology for sintering mechanism characterization

The characterization of the initial stage of the sintering mechanism corresponds first to the determination of the activation energy Q of mass transport or reaction, and secondly to the determination of the P-coefficient, giving rise to the kinetic limiting process. The anisothermal and stepwise isothermal approaches used in this study are all developed in the framework of Eq 1 with the assumption that the function K_0 (Eq 2) only depends on temperature T and not of coordination number Z and density D (Eq 7).

3.1. Anisothermal methodology

Anisothermal methodologies are based on shrinkage measurements carried out at constant rate of heating α (CRH methodology). Different kinetic equations have been developed [23,27] to extract from the experimental data the activation energy Q and the transport coefficient P [23,28,29,65]. In the SI, the solving steps proposed by Woolfrey and Bannister [23] are described, which from Eq 1 lead to Eq 8 and Eq 9, and allow determination of P and Q from CRH experiments.

$$\ln(\varepsilon) = -\frac{1}{P} ln(\alpha) + C_1 \qquad \textit{Eq 8}$$

$$T^2 \varepsilon'(t) = \frac{\alpha Q}{PR} \varepsilon \qquad \textit{Eq 9}$$

First, to determine the P-coefficient, several experiments, using various values of heating rate α, must be conducted in order to plot $ln(\varepsilon)$ vs $ln(\alpha)$ at a given absolute temperature T, and to deduce from the straight line the P-coefficient (Eq 8).

For each constant heating rate experiment, the plot $T^2\varepsilon'(t)$ vs ε gives a straight line with a slope close to $\alpha Q/PR$ allowing the evaluation of the activation energy Q by considering the value of the P-coefficient determined from Eq 8.

3.2. Stepwise isothermal methodology

For constant temperature experiments, the P-coefficient can be directly determined from the shrinkage rate Eq 1 by plotting $ln\left(\varepsilon'(t)\right)$ vs $ln(\varepsilon)$, the slope of the straight line being $(1-P)$ (see Eq 10 with C_2 a constant). In Figure 5B, the straight lines for two isothermal segments are illustrated.

$$ln(\varepsilon'(t)) = (1 - P)ln(\varepsilon) + C_2 \qquad \textit{Eq 10}$$

The activation energy can be evaluated from different isothermal experiments using various temperatures. In this work, we have selected the stepwise isothermal method, which presents the advantage of determining the activation energy from a unique experiment. This methodology was initiated by Dorn [66] , and applied by Bacmann and Cizeron [67] to evaluate the activation energy of rheological behavior. It was also applied to investigate i) the kinetics of thermal decomposition from controlled transformation rate data [68–70] or from thermogravimetry data [71] and of relevance to this study ii) the sintering kinetics from dilatometry data [67]. Here, the principle associated with this methodology is to bring the powder compact successively to different isothermal conditions characterized by the temperatures T_1 and T_2, and to record the subsequent changes of the shrinkage behavior (Figure 5A). The plot $ln(\varepsilon'(t))$ vs $ln(\varepsilon)$ (Figure 5B) is thus characterized by two straight lines corresponding to the two isotherms T_1 and T_2 in consistency with Eq 10. From the isothermal segment T_1, the shrinkage rate $\varepsilon_1'(t)$ is directly determined at the end point 1 just before the temperature rise. The shrinkage rate $\varepsilon_2'(t)$ is determined at the time when the isotherm T_2 is reached. If the temperature jump is rapid enough, the shrinkage rates $\varepsilon_1'(t)$ and $\varepsilon_2'(t)$ are determined at the same shrinkage ε where the densifying material is characterized by the same coordination number Z and the density D. In these conditions, the K_0 function only depends on temperature T. From the (ln($\varepsilon_1'(t)$), ln($\varepsilon_2'(t)$)) couple and applying Eq 1, the activation energy Q can be defined by:

$$Q = R\frac{T_1T_2}{(T_1 - T_2)}ln\left(\frac{\varepsilon_1'(t)}{\varepsilon_2'(t)}\right) \; if \; \frac{Q(T_1 - T_2)}{RT_1T_2} \gg \ln\left(\frac{T_2}{T_1}\right) \qquad \textit{Eq 11}$$

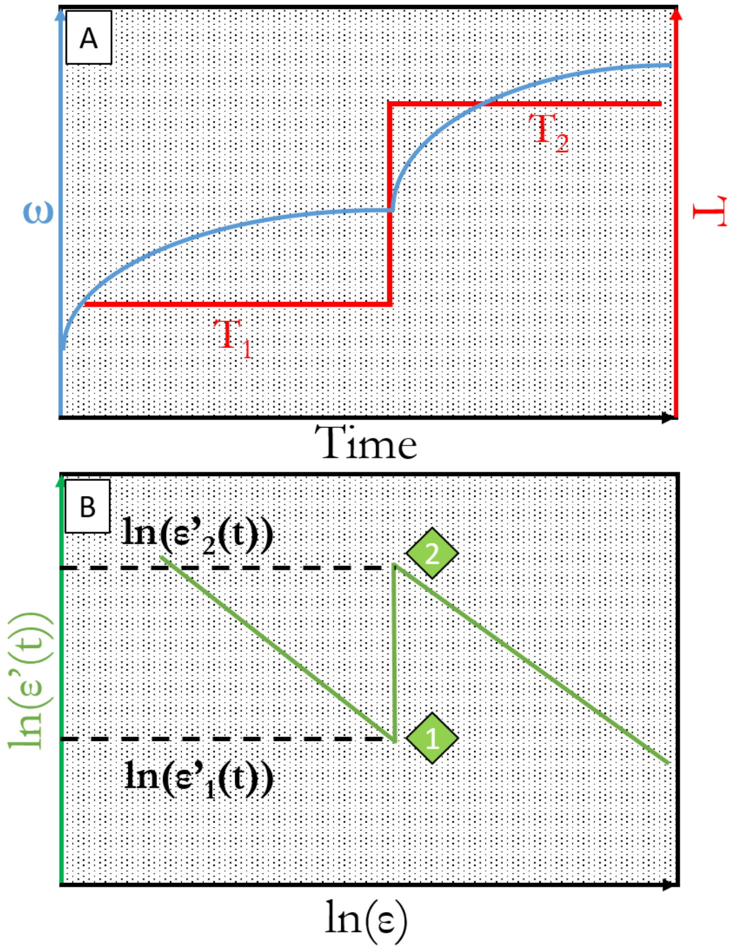

Figure 5 : Schematic of the stepwise isothermal methodology allowing the determination of the transport mechanism coefficient *P* and activation energy *Q* from a single experiment. A: Red curve: Temperature evolution; Blue curve: shrinkage evolution. B: Green curve: Shrinkage rate evolution.

4. Experimental Details

Commercial ZnO powder (NanoTek®, Alfa Aesar) with a particle size ranging between 40 to 100 nm was selected as a starting powder. The solvent used is a 2 M solution of acetic acid prepared from the dilution of glacial acetic acid (99.8 %, Acros Organics, 222140010). Densification of ZnO by a low-temperature process, such as hydrothermal sintering or cold sintering, was shown to be optimal with acetic acid as the liquid phase [38,40,72]. For each hydrothermal sintering experiment, 1 g of ZnO powder was mixed with 10 wt% of 2 M acetic acid solution for 5 min in an agate mortar. The solvent weight fraction was selected to limit extrusion of the powder during the first pressing step at room temperature and during sintering. The mixture was first introduced in the hydrothermal sintering reactor, constituted of a 10 mm diameter Inconel die with close-fitting pistons using Teflon® seals to keep the system closed and retain the expelled liquid phase in dedicated reservoirs during densification. Then the sintering die was pressed under 320 MPa at room temperature for 5 min to allow further particle rearrangement. Note that the relative density at the beginning of heating ramp was evaluated to 68% by Archimedes' principle in ethanol. Then the system was kept under pressure and the temperature raised up to 150 °C, using different heating ramps. Finally, the pressure is controlled by the automatic device (720 $N.min^{-1}$; 9.2 $MPa.min^{-1}$) to corroborate the natural decrease of the system temperature.

4.1. *In situ* dilatometry

In order to measure the linear shrinkage of the pellet as a function of temperature and time, a device was specifically designed to follow the displacement in compression of the pistons located in the hydrothermal sintering reactor. This displacement is measured as a function of both the applied force and the temperature (see SI part S3). This bench allows the generation of a maximum Force of 100 kN, to impose a speed of 0.05 $\mu m.min^{-1}$ up to 800 $mm.min^{-1}$ with a resolution of the positioning of ± 0.1 µm, allowing us to follow the expansion / retraction of the sample placed in this reactor in an extremely precise way. The force measurement sensor (100 kN class 0.5) allows a measurement to ± 0.5 % of the value read from 0.5 % to 100 % of the full scale. For all hydrothermal experiments, calibration (die without mixture) was performed to subtract the linear displacement caused by the sintering die thermal expansion.

For the anisothermal experiments, the procedure described above was followed. Three heating ramps were selected, 0.78, 1.56, and 2.80 $°C.min^{-1}$ from 20 to 150 °C. Slow heating ramps were selected to limit the extrusion of the powder during hydrothermal sintering. This extrinsic parameter could lead to inaccurate measurements of the shrinkage, especially during the early stages of sintering considered under this investigation.

For the stepwise isothermal experiments (section 3.2), 20 min isotherms were performed at the selected temperatures 32, 42, 52, 62, and 72 °C. The heating ramp used before 32 °C, after 72 °C, and between two successive isotherms was lower than 1 °C.min^{-1} because of the heating kinetics of the autoclave. The shrinkage was measured during each experiment.

5. Results

5.1. Anisothermal experiments

The anisothermal sintering was investigated following the CRH method, which is used in conventional sintering to analyze the initial stage of sintering. CRH experiments consist of measuring the shrinkage (ε) at different heating rates (α), and allowing to determination of the energy activation (Q) and the transport coefficient (P) [23,28,29,65]. Figure 6 shows a typical evolution of the temperature and the shrinkage as a function of time for the hydrothermal sintering of ZnO, considering a heating rate of 0.78 °C.min^{-1}. As mentioned in the experimental section, an external pressure of 320 MPa was kept constant for 5 minutes before raising the temperature and during all the experiments. The maximum shrinkage corresponds to 27 % of the initial length of the sample. The initial length of the sample was measured at the onset of the temperature increase. Similar value of shrinkage is obtained for the experiments performed with heating ramps of 1.57 and 2.80 °C.min^{-1} (see SI Figure S1 and S2).

The CRH method is valid when the heating ramp is constant over the temperature range considered. For each heating ramp, the ranges of temperature with constant heating have been identified and the data accordingly recorded: 26 - 149 °C for 0.78 °C.min^{-1}, 33 - 146 °C for 1.57 °C.min^{-1}, and 40 - 143 °C for 2.80 °C.min^{-1}.

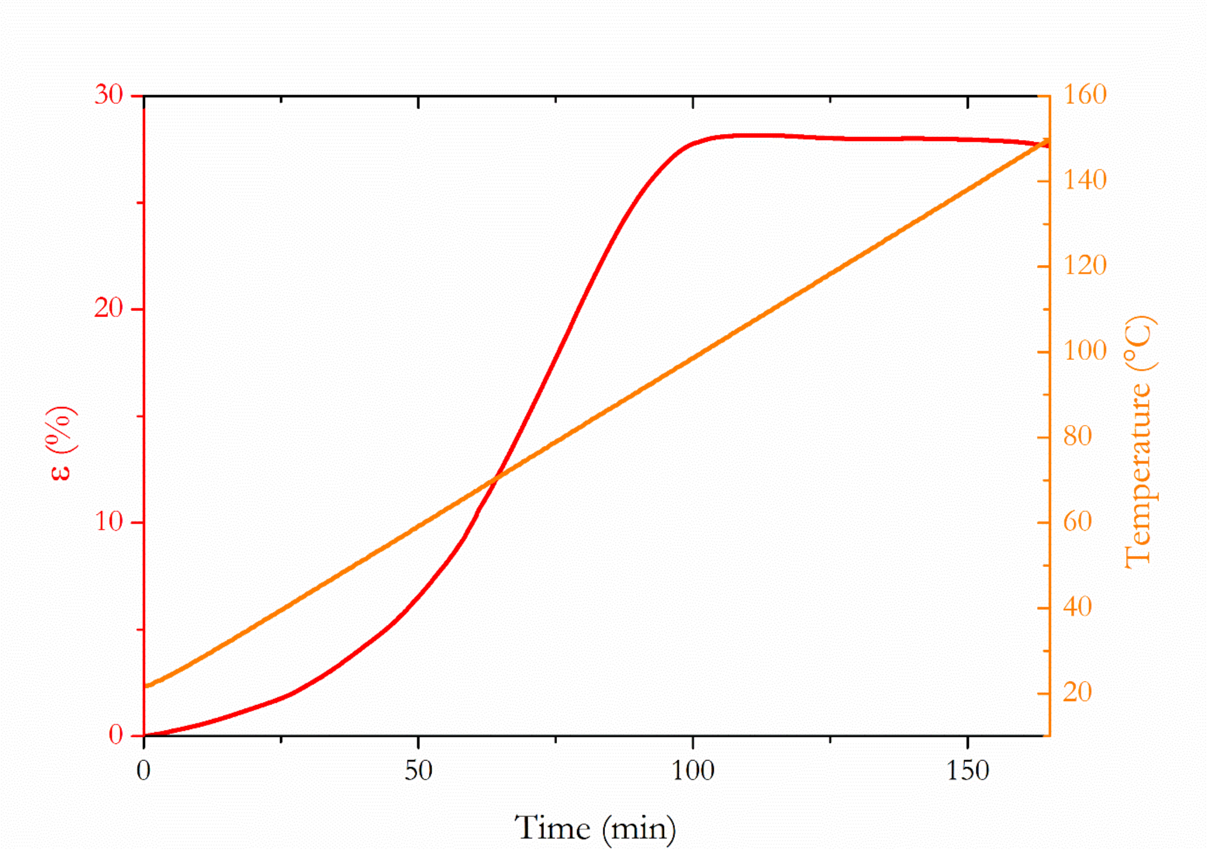

Figure 6 : Shrinkage and temperature evolutions during ZnO anisothermal hydrothermal sintering until 150 °C with a heating ramp of 0.78 °C.min^{-1}.

5.1.1. Validity criteria

Considering that the transport coefficient P and the activation energy Q are identified from data of three different heating ramps, we have to make sure of the consistency of these sintering characteristics at different heating ramps. The way to verify is to draw the plots $\left(T^2\varepsilon'(t)\right)/\alpha$ vs ε for the three heating ramps, which should give rise to superimposed linear evolutions characterized by the same Q/P ratio (Eq 11). This is confirmed and can be observed in Figure S3 (SI). By setting as a validity criterion the shrinkage domain where the evolution of $T^2\ \varepsilon'(t)$ vs ε is perfectly linear for each heating ramp (Figure 7), an accurate determination of both the transport coefficient P and the activation energy Q can be thus expected. These domains are highlighted in Figure 7 by the superimposition of the experimental curves with linear evolutions characterized by dashed lines. They are precisely defined in Table 1 with the corresponding temperature intervals.

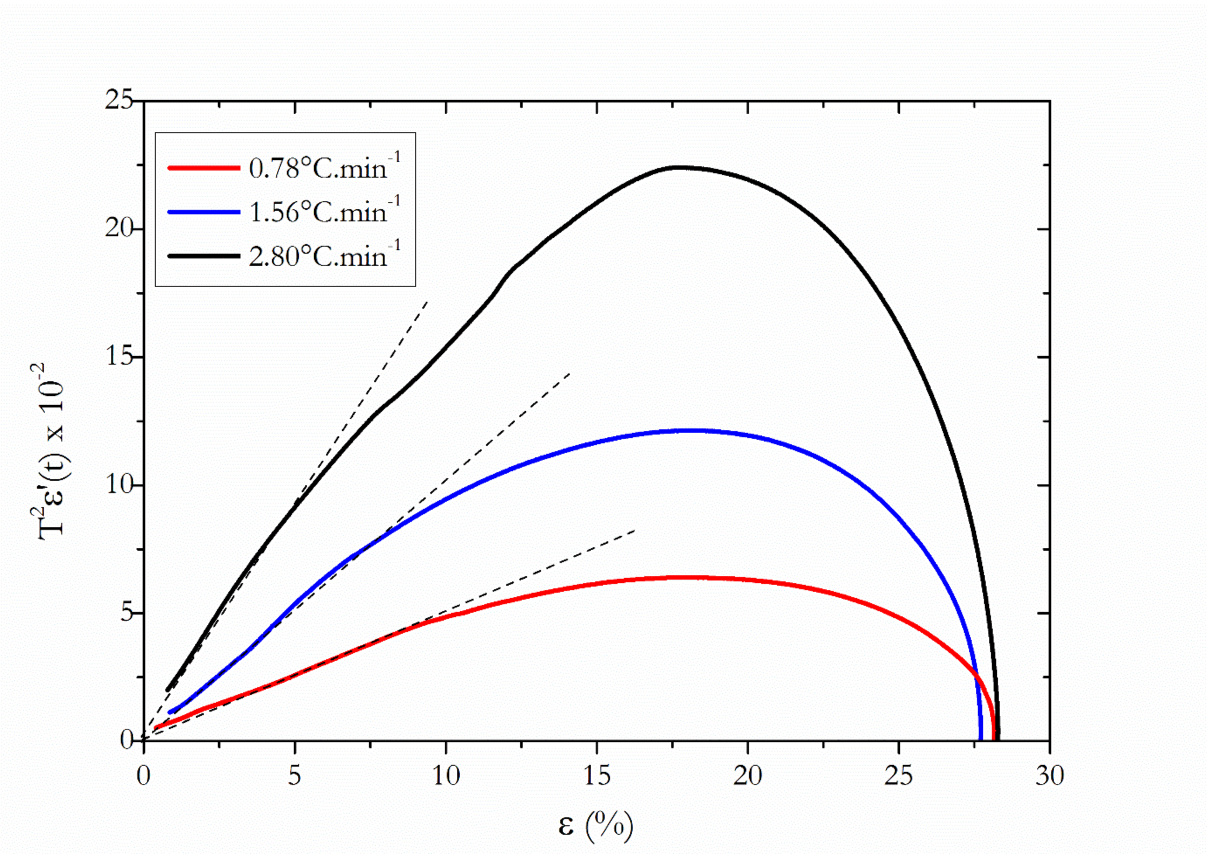

Figure 7 : Plot of $T^2\varepsilon'(t)$ as a function of shrinkage at different heating ramps

Table 1 : Shrinkage intervals and related temperature intervals corresponding to the validity criteria for accurate kinetic exploitation of the experimental data

Heating ramp (°C.min^{-1})	0.78	1.56	2.80
Shrinkage interval (%)	1.5 – 8.6	0.9 – 8.0	1.1 – 5.6
Temperature interval (°C)	37 - 64	33 - 69	40 - 70

Note that the upper limit of these shrinkage domains is lower than 10 %, a value above which the sintering kinetics do not characterize anymore the initial stage of sintering process.

5.1.2. Determination of the transport coefficient P

The coefficient of transport mechanism P, is obtained from Eq 9, by plotting $ln(\varepsilon)$ as a function of $ln(\alpha)$ for a given temperature. The way to obtain such representation requires an intermediate graph where $ln(\varepsilon)$ is plotted as a function of $1000/T$ for the three heating ramps (Figure 8). Note, that the slopes of the curves corresponding to each heating ramp are almost parallel to each other since Eq S6, $ln(\varepsilon) = -1/P\left(Q/RT + ln(T)\right) + C$ gives rise to a straight line when $Q/RT \gg ln(T)$. For a given temperature (Figure 8), it is thus possible to determine the three points $(ln(\varepsilon), ln(\alpha))$, which are then plotted in Figure 9 for each temperature. Then, the transport mechanism coefficient P is calculated from the slopes of the straight lines corresponding to $-1/P$ (Eq 8). The values of these obtained coefficients reported in Table 2 vary from 1.69 at 50 °C to 4.77 at 100 °C. Within the defined shrinkage intervals according to the validity criterion (Table 1), the values of the coefficient P are only representative between 50 and 70 °C with P = 1.9 ± 0.2. The value at 40°C for the fastest ramp has not been used to calculate P because it is only from this temperature that the temperature ramp becomes constant.

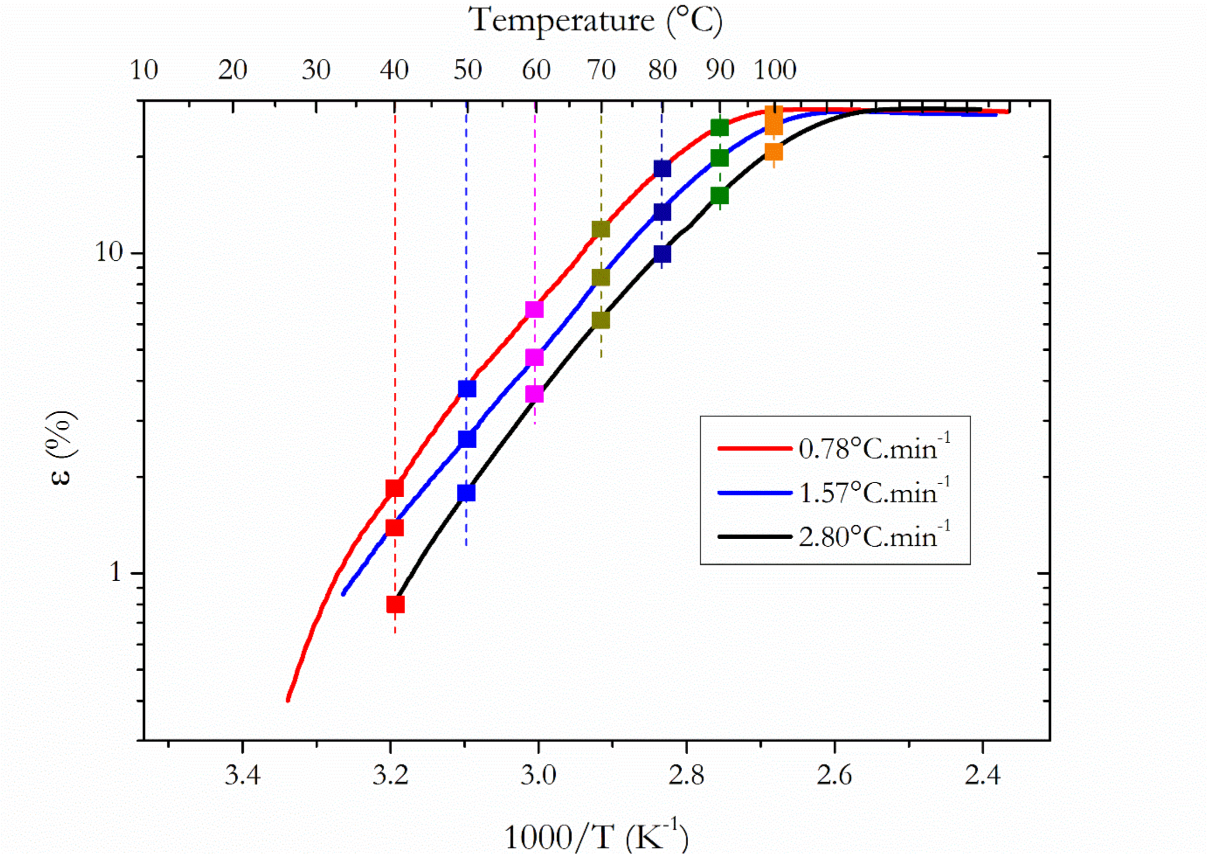

Figure 8 : Evolution of shrinkage in log scale as a function of temperature.

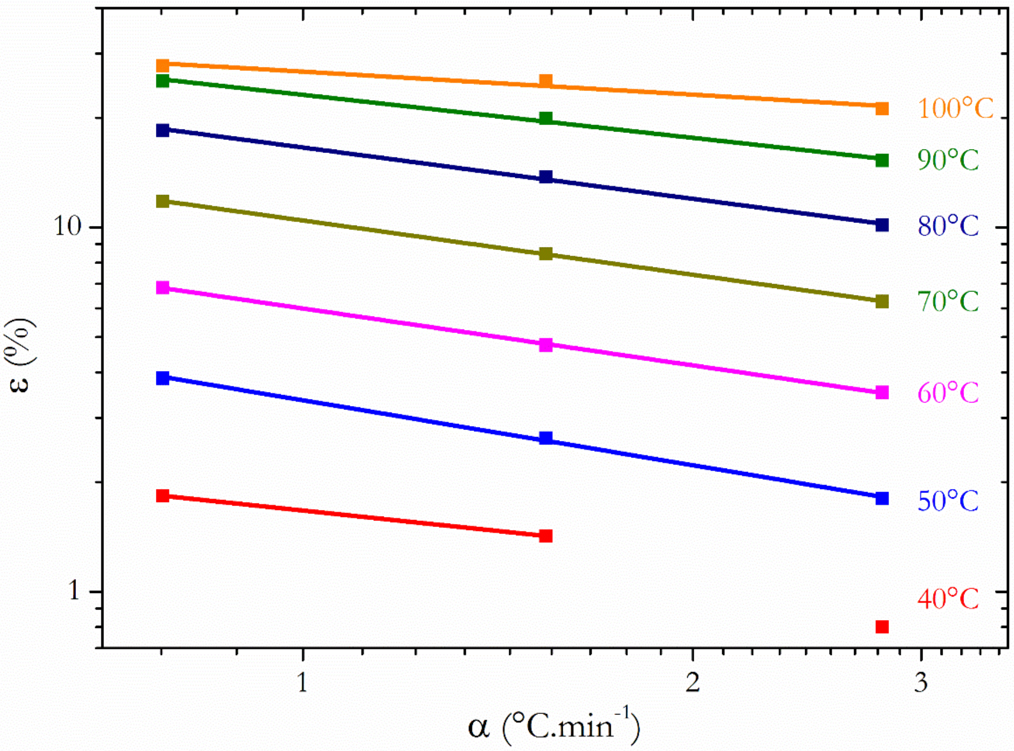

Figure 9 : Effect of heating rate on shrinkage at specific temperatures for CRH sintering of ZnO.

Table 2 : Determination of the P-coefficient as a function of temperature. The framed part highlights dataset corresponding the validation criterion

Temperature(°C)	40	50	60	70	80	90	100
P	2.68	1.69±0.07	1.93±0.04	2.02±0.02	2.14±0.11	2.55±0.19	4.77±1.00

5.1.3. Determination of the activation energy

As described in section 3.1, the value of the activation energy Q can be determined from the plot $T^2\varepsilon'(t)$ vs ε already shown in Figure 7. The Q/P ratio for each heating ramp is deduced from the slope of the corresponding straight line (Figure 7). The obtained values are reported in Table 3. From the mean value of the P-coefficient previously obtained, P = 1.9 ± 0.2, the activation energy is determined for each heating ramp. The obtained values are presented in Table 3. The value of the activation energy of this first stage of sintering under the hydrothermal sintering conditions is thus Q = 98 ± 11 kJ.mol^{-1}.

Table 3 : Activation energy for different heating ramps of ZnO sintering.

Heating ramp (°C.min^{-1})	Q/P	Q (kJ.mol^{-1})
0.78	49.2 ± 0.6	93.5 ± 11.0
1.57	54.7 ± 0.4	103.9 ± 11.6
2.80	50.5 ± 0.2	95.9 ± 10.5

5.2. Stepwise Isothermal experiment

The stepwise isothermal methodology applied to sintering analysis is described in section 3.2. It is pointed out that the determination of the transport mechanism coefficient P and the activation energy Q can be obtained from a single experiment. The imposed thermal cycle is shown in Figure 10, starting from 20 °C to 150 °C, with isothermal steps of 20 min every 10 °C, between which the heating ramp is lower than 1 °C.min^{-1}. From the shrinkage curve, we notice that five isotherms concern the first sintering stage (below 10 % shrinkage). If a larger number of isotherms would have allowed a better quantification of the evolution of the couple $(P\ ;Q)$ during this first stage, long dwell times were preferred to enable the system to equilibrate and thus to allow an accurate measurement of the decrease in shrinkage rate for kinetics analysis. Working with a low temperature process induces issues related to the temperature regulation, as observed in Figure 10 (zoom focused between two isotherms).

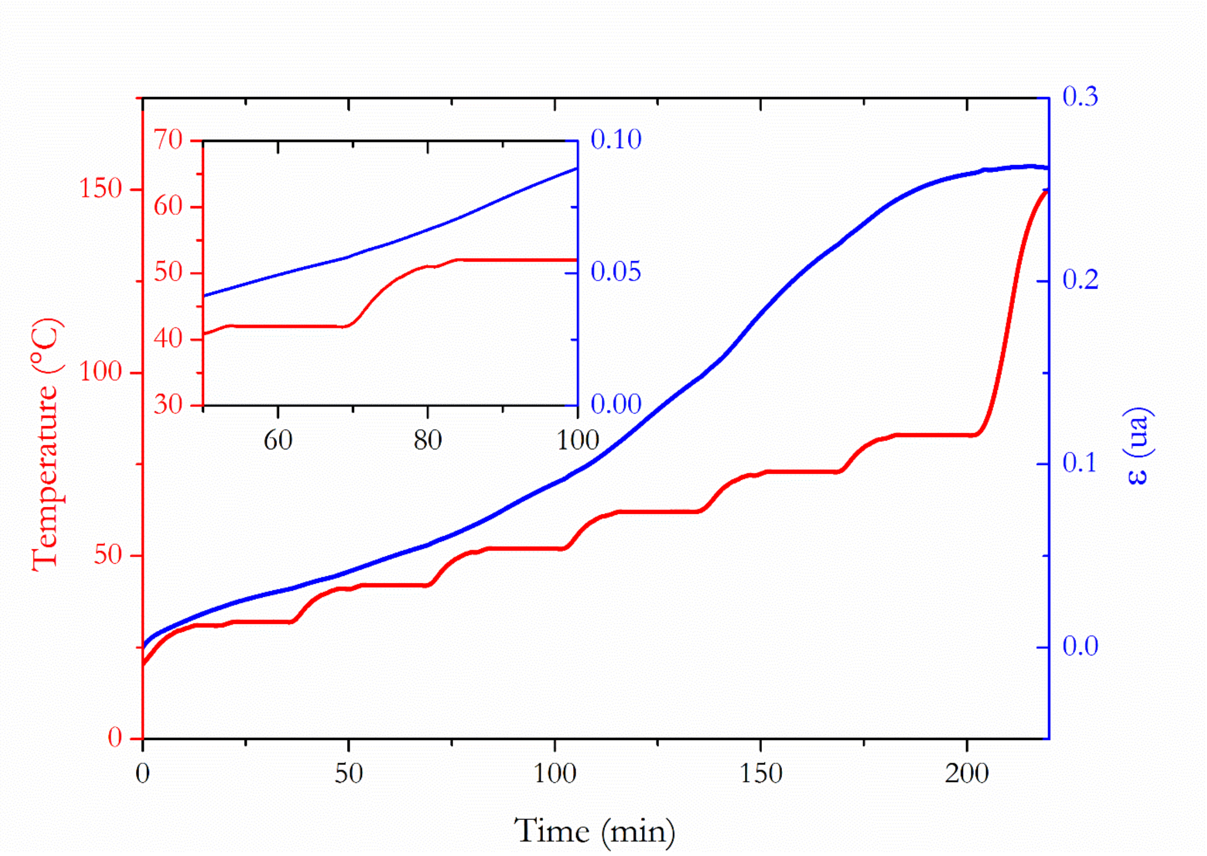

Figure 10 : Evolution of temperature and shrinkage as a function of time during the stepwise isothermal experiment and a zoom that shows the temperature regulation between two isotherms.

5.2.1 Determination of the transport mechanism coefficient

The P-coefficient is determined from the plot $ln(\varepsilon'(t))$ vs $ln(\varepsilon)$, as shown schematically in Figure 11. The slope of the straight line relative to each isotherm corresponds to $1 - P$ (see Eq 10 and Figure 5), wich are reported in the Table 4 as corresponding P-value. Figure 5 illustrates the cycles used to reach an ideal temperature regulation with a rapid jump from an isotherm to another. As previously noticed, there is a large time interval between two successive isotherms (zoom in Figure 10), so only the segment corresponding to each regulated temperature was drawn in Figure 11 . The full representation is provided in the SI (Figure S4). It should be noted that the experimental log-log plot is not perfectly linear, as would be expected based on the theory. This can be explained by uncertainties related to the sensitivity of the device. Furthermore, the contribution of additional mechanisms, such as dissolution followed by a rearrangement, cannot be ruled out. From these isothermal segments, the $(1 - P)$ slope can nevertheless be determined with an acceptable accuracy

(Figure 11). Except for the P-value obtained at T = 32 °C, below 10 % shrinkage where a constant value P = 2.1 ± 0.1 is obtained. The values obtained at 32 and 72 °C, respectively 2.48 and 3.63, significantly deviate from the P = 2.1 ± 0.1 value and are thus expected not to characterize the initial stage of sintering.

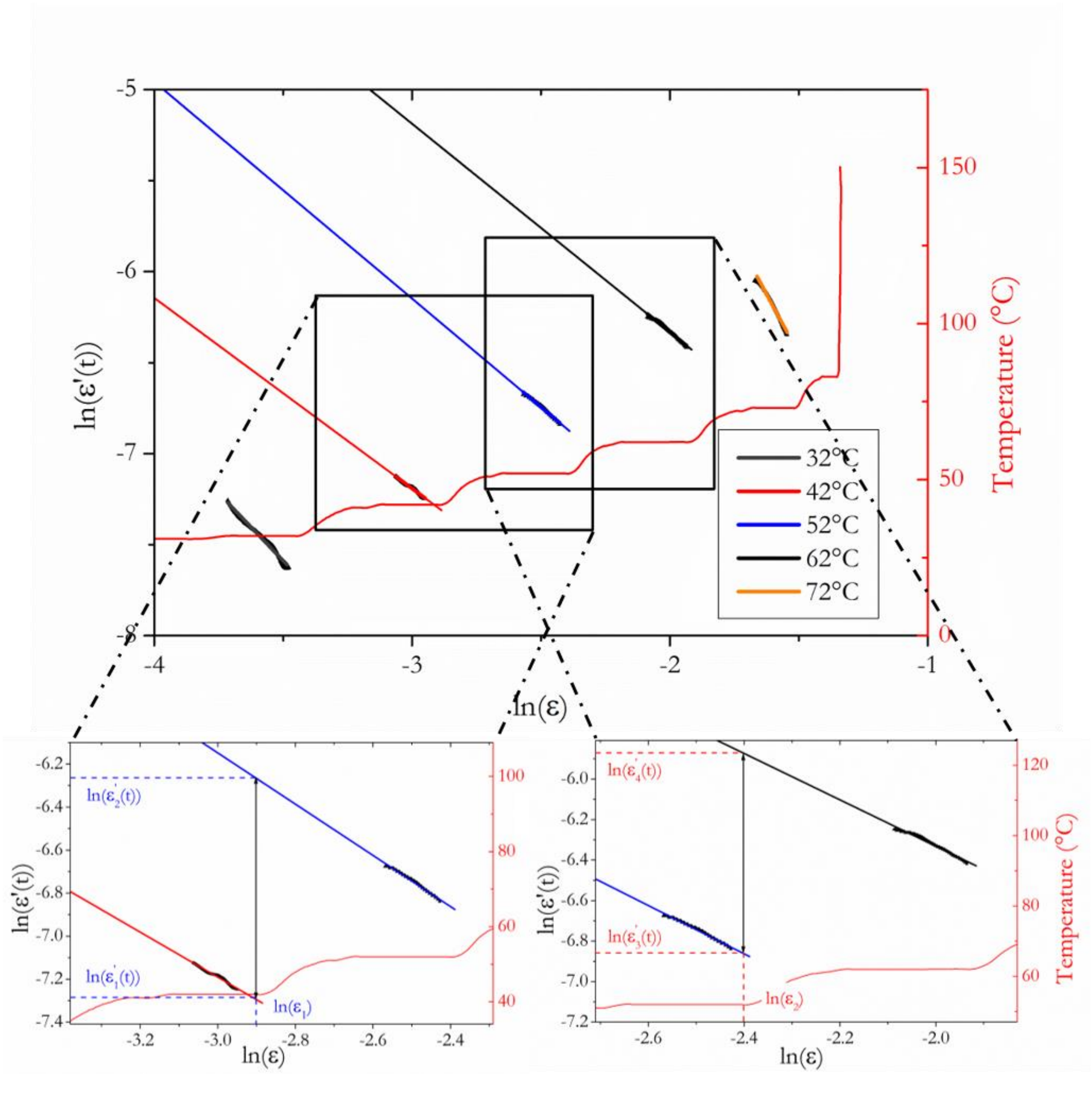

Figure 11 : The evolution of experimental (black dots) and the extrapolated (colored line) evolution of $ln(\varepsilon'(t))$ as a function of $ln(\varepsilon)$ by the stepwise isothermal experiment, allowing calculation of the activation energy Q from two isotherms (Eq 11). A zoom is proposed in the range 42 and 52 °C and 52 and 62 °C for sake of clarity.

Table 4 : Values of the P-coefficient deduced from the slope $\left(ln\left(\varepsilon'(t)\right); ln(\varepsilon)\right)$ characterizing each isotherms of the stepwise isothermal experiment (Eq 10) and drawn in Figure 11. The uncertainties are the standard deviation of the linear deviation of the linear regression. The framed part corresponds to the validity criterion.

TEMPERATURE (°C)	**SLOPE**	**P**
32	-1.48	2.48 ± 0.01
42	-1.05	2.05 ± 0.01
52	-1.19	2.19 ± 0.01
62	-1.15	2.15 ± 0.01
72	-2.63	3.63 ± 0.01

5.2.2 Determination of the activation energy

With the stepwise isothermal approach, the activation energy calculation is based on the determination of two shrinkage rates $\varepsilon_1'(t)$ and $\varepsilon_2'(t)$ (related to the isotherms T_1 and T_2) for the same shrinkage ε (section 3.2, Figure 5). As previously discussed from Figure 10, since the temperature jump is experimentally not rapid enough, the two shrinkage rates are consequently determined for a large shrinkage interval (Figure 11). To overcome such a problem, and as an example, considering the temperature interval from T_1 = 42 °C to T_2 = 52 °C, the shrinkage rate $\varepsilon_2'(t)$ is obtained from the extrapolation of the isothermal segment at T_2, for exactly the same shrinkage ε of point 1 (Figure 11). From the (T_1, T_2) and ($\varepsilon_1'(t)$, $\varepsilon_2'(t)$) couples, the activation energy can thus be determined using Eq 11. This method allows calculation of the activation energy for all pairs of isotherms. The results are shown in Table 5. As for the values of P, we also note that the two activation energy values obtained in the 42 °C - 62 °C temperature range are very close Q = 89 ± 3 kJ.mol^{-1}, confirming the consistency of the method.

Table 5 : Activation energies defined from the different isotherm couples imposed during the densification of ZnO by hydrothermal sintering. The framed part corresponds to the validity criterion. The uncertainties are calculated from that of temperature (±0.01 °C) and piston displacement given by the device precision (see section 4.1)

Temperature (°C)	32 - 42	42 - 52	52 - 62	62 - 72
Q (kJ.mol^{-1})	73.9 ± 3.8	88.3 ± 2.8	89.4 ± 2.0	106.2 ± 1.5

6 Discussion

6.1 Comparative study of anisothermal and stepwise isothermal approaches

The linear shrinkage of the ZnO pellets was considered as a function of time and was recorded during the first stage of sintering. Such *in situ* dilatometry under the hydrothermal sintering has allowed testing of both the anisothermal and stepwise isothermal methodologies for sintering mechanisms characterizations (Section 5.1 and 5.2). The values of P-coefficients and activation energies Q of mass transport or reaction are collected and shown in Table 6 and Table 7, respectively, for both approaches and within the temperature range defined, considering the first stage of sintering. The uncertainty values of the P-coefficient over different temperature ranges (Table 6) are smaller and more uniform for the stepwise isothermal approach compared to the anisothermal approach. This is consistent with the way they are determined at each temperature, from a unique experiment and from three heating ramp experiments for the stepwise isothermal and anisothermal approaches, respectively. Similarly, the dispersion on the three selected values of the P-coefficient around the average value is lower (P = 2.1 ± 0.1) for the stepwise isothermal approach than for the anisothermal approach (P = 1.9 ± 0.2). Nevertheless, the average values obtained considering the two approaches are very close, giving rise to a reliable value, P = 2, for the coefficient related to the mechanism of the initial stage sintering.

Concerning the activation energy of mass transport or reaction, average values of Q are (89 ± 3) kJ.mol^{-1} from stepwise isothermal and (98 ± 11) kJ.mol^{-1} from anisothermal approaches. A smaller uncertainty is also obtained for the stepwise isothermal approach compared to the anisothermal one (Table 7). The main reason is that this activation energy is calculated independently of the P-coefficient (Eq 11) for the former, whereas it is deduced from the quotient Q/P (Eq 9) for the latter. In this case, the P-coefficient is obtained with a relative uncertainty of about 10 % over the temperature range, which corresponds to linear part of the $(T^2\ \varepsilon'(t); \varepsilon)$ graph (see Figure 7 and Table 1). Moreover, the advantage of the stepwise isothermal approach is to be free of any assumption regarding the coordination number Z and the density D must be emphasized (Eq 7). Here again, the values of the activation energy obtained using the two approaches are relatively close, which is a good guarantee of the consistency and reliability of the results. It can be assumed that the limiting kinetics mechanism of the initial stage of sintering is characterized by an activation energy Q = 90 kJ.mol^{-1} and a coefficient P = 2. As discussed previously, these values are sufficiently reliable to discuss the mass transport or reaction mechanisms involved in the first stage of ZnO sintering by hydrothermal sintering.

Table 6 : Comparative values of the P-coefficient, related to mass transport or reaction, obtained from stepwise isothermal and anisothermal methods

Temperature (°C)	$P_{isotherm}$	$P_{anisotherm}$
42	2.05 ± 0.01	-
52	2.19 ± 0.01	1.69 ± 0.07
62	2.15 ± 0.01	1.93 ± 0.04
72	-	2.02 ± 0.02

Table 7 : Comparative values of activation energies Q, related to mass transport or reaction, obtained from stepwise isothermal and anisothermal methods

	RAMP (°C.MIN^{-1})	**Q (KJ.MOL^{-1})**
ANISOTHERM	0.78	93.5 ± 11.0
	1.57	103.9 ± 11.6
	2.80	95.9 ± 10.5
ISOTHERM	Temperature (°C)	Q (kJ.mol^{-1})
	42 - 52	88.3 ± 2.8
	52 - 62	89.4 ± 2.0

6.2 Identification of the sintering mechanisms

The value of the activation energy of densification is representative of a transport or reaction mechanism, which depends on the material, the microstructure, the presence of defects preferentially located at surface or grain boundaries, and the sintering conditions with, in particular, the important role of the solvent phase in contact with particles under the initial stages of sintering. Considering conventional sintering of ZnO under air, the activation energy is 253 kJ.mol^{-1}, and the associated mechanism is ascribed to volume diffusion [73]. When a uniaxial stress is applied during sintering, the activation energy is lowered and the location of mass transport impacted. Indeed, the obtained values are 190 kJ.mol^{-1} for high pressure sintering and 215 kJ.mol^{-1} for electric field assisted sintering (FAST/SPS), and in each case the transport mechanism has been identified as grain boundary diffusion [64]. Furthermore, when the ZnO powder is hydrated with 1.6 wt% water and sintered by FAST/SPS, the activation energy is further decreased to 130 kJ.mol^{-1} [74]. The studies mentioned above are all based on isothermal approaches, and they highlight the influence of the sintering conditions and process on the evolution of activation energy of sintering and the mass transport mechanisms associated.

The anisothermal approach has already been applied to ZnO conventional sintering, the obtained activation energy is 316 - 329 kJ.mol^{-1} when a micrometer grain size powder is used, and 201 kJ.mol^{-1} [75] for a nanometer grain size powder [76]. Whatever the grain size, the mass transport mechanism was attributed to volume diffusion. More recently, a kinetic study has been performed on ZnO sintered by CSP [40]. The authors reported activation energies drastically decreased compared to those reported for conventional or high pressure sintering (HIP, FAST/SPS); the obtained value was 50 kJ.mol^{-1}. Such a low value reflects a new densification mechanism involving different diffusion paths and for which the solvent plays a key role in controlling the kinetics of dissolution-precipitation creep mechanism.

The activation energy value obtained for the densification of ZnO by hydrothermal sintering in presence of acetic acid is close to 90 kJ.mol^{-1}, a value higher than that obtained by CSP but lower than the one reported when hydrated ZnO is sintered by FAST/SPS. Referring to the mechanisms involved in solid state sintering (Figure 1), the obtained value of activation energy allows exclusion of the volume diffusion mechanism (P = 2) or the diffusion creep at the grain boundary by reverse flux of vacancies (P = 3 on Figure 1), which are, as discussed above, characterized by activation energies higher than 200 kJ.mol^{-1}. Such a low value of activation energy in the case of HSS better fits with the presence of the reactive solvent layer at the contact between particles (Figure 3). Nevertheless, diffusion through inter-particle film is characterized by a coefficient P = 3 [2,56] (Figure 3 — pathway 2) and is therefore not consistent with the value P = 2 obtained in this study. This latter value thus suggests that the limiting kinetic process is rather the dissolution reaction at the grain boundary and contact point in reference to literature [2,56] (Figure 3 — mechanism 1). Note that the initial grain sliding mechanism associated with particle shrinkage (see section 2.2 and Figure 4) is assumed here to be sufficiently fast that it does not significantly interfere with this dissolution reaction limiting process. However, it is clear that when rough surfaces undergo dissolution, particles sliding may still occur to a small extent. Roughness and edge sites that develop on the grain boundaries should be considered, as there is a lot of evidence in CSP TEM studies of such roughness [38]. Another contribution would be the local curvatures and roughness that could lead to variation of point defect concentration along these boundaries. These local variations are not considered here, but we approximate an enhanced mass transport with fluxes of solute.

Therefore, even if some coupling of contributions has to be considered, the mechanism can still be rate limited by the dissolution reaction process. This is supported by i) the consistency of the obtained Q value with those of other oxides dissolution [77,78] (in the range 40 to 100 $kJ.mol^{-1}$), and ii) by discarding the unique contribution of solute diffusion within the solvent, which would correspond to an activation energy much lower around 20 $kJ.mol^{-1}$ [79]. However, it is worth noting that the activation energy of dissolution of ZnO in 1 M acetic acid is 43 $kJ.mol^{-1}$ [80], which is a factor of two lower than the one evaluated for hydrothermal sintering. Indeed, The dissolution/precipitation reaction of ZnO in acetic acid is a complex reaction composed of three successive steps (detailed in SI-S5): i) the dissolution leading to the formation of Zn^{2+} [77,81], ii) a complexation of Zn^{2+} with acetates to form crystalline zinc acetate [82] and which was confirmed by a ReaxFF dynamic atomic simulation [38,83], and iii) the precipitation of ZnO through the decomposition of the acetates [84]. More generally, dissolution controlled kinetics for ZnO and acid solutions have been studied from a number of investigations and found to be between 38 $kJ.mol^{-1}$ to 48 $kJ.mol^{-1}$ [85–87].

The comparative study between ZnO sintering by CSP (open system) and hydrothermal sintering (closed system) has highlighted a difference in surface reactivity and precipitation paths, depending on the sintering process [38]. The precipitation of a crystalline zinc acetate hydrate phase during hydrothermal sintering (not observed for cold sintering in similar experimental conditions) likely points to the formation of different intermediate chemical species during dissolution, [82] as well as reaction kinetics following the open *vs* closed nature of these systems, which may be factors explaining a higher Q value. Furthermore, Zeumault and Volkman have recently shown that activation energies of approximatively 90 $kJ.mol^{-1}$ may be related to the zinc acetate to ZnO transformation at low heating rates [88]. Further investigations are required to go deeper on this point.

To sum up and in the specific framework of this study, the first stage of hydrothermal sintering involves the sequential dissolution / diffusion / precipitation mechanisms, among which is the most likely limiting process dissolution reaction. In addition, the solute diffusion through the interparticle film and sliding phenomena could also be intermingled, as recently highlighted on the creep deformation of soft rocks in geotechnical engineering [89–95]. So, in the earlier stages of densification and at low temperatures under HSS, we anticipate that not only is the densification due to the mass transport processes that are outlined in Figure 3, but we could also anticipate interfacial necks to be formed and broken in the early stages under sliding and rearrangement as densification proceeds, and therefore the activation energies would be expected to be greater than just rate limiting processes such as dissolution.

7 Conclusions

The present kinetic study of hydro-solvothermal sintering of zinc oxide was conducted within the framework of the two-particle kinetic equation, considering surface tension and applied pressure as contributions to the driving force. The study is limited to the first stage of sintering (less than 10% shrinkage). This basic equation was demonstrated to be valid for 3D compacts if the sliding mechanism of the particles over each other is easy enough to induce, from a uniaxial loading, an isostatic like pressing without any deformation of the particles. Then this two-particle kinetic equation, shown to be suitable to the hydrothermal sintering, was used to determine sintering mechanism (activation energy of the transport or reaction and a power law coefficient P related to the shrinkage variable).

Two methodologies were investigated to extract mechanisms and energetics in this early stage of hydrothermal sintering, the first one based on anisothermal experiments, and a less conventional one based on stepwise isothermal experiments. These kinetic investigations were performed thanks to a dilatometer specifically designed to allow recording *in situ* the linear shrinkage of ZnO pellet as a function of time. The results obtained while contrasting the two methodologies were shown as coherent. The activation energy values (90 kJ.mol^{-1}) and mechanism coefficient (P = 2) obtained are very close, which is a good guarantee of the consistency and reliability of the results. The relevance of the stepwise isothermal approach about accuracy has also been highlighted, considering that the activation energy is calculated independently of the mechanism coefficient and for the same material density.

As a result, hypotheses relative to the limiting mechanisms of the sintering process in the first stages of sintering have been proposed. The low activation energy values obtained and the value of the mechanism coefficient close to 2 may be indicative of a dissolution reaction-controlled mechanism, if referring to the coefficient introduced by Kingery [2]. Then the activation energy values are consistent with those of the dissolution mechanism of some oxides, but higher than those of ZnO in acetic acid. This suggests that in the early stages of densification by HSS, additional processes coupled to the dissolution process and arising from the surface reactivity may occur. In addition to that, the zinc acetate to ZnO transformation at low heating rates may be another contributing factor for higher activation energies in the ZnO / Zn-acetate / acetic acid system.

This first insight in mechanisms and their associated activation energy of hydrothermal sintering clearly explained the much lower temperature range than the ones targeted in conventional or advanced sintering, such as SPS. Nevertheless, the consistency of our results to propose the dissolution reaction as the most likely limiting process is also related to the choice of the material / solvent couple, the grain size and shape, the particle size distribution, the volume fraction of the solvent in the porosity, and the value of the applied pressure.

As a related perspective, to study the overall strain evolution, phenomenological models developed within the framework of pressure solution creep would be appropriate [51,90–93,95,96].

The pressure solution creep studies point to strain rates that are driven by the processes: (1) dissolution of material at the highly stressed grain contact points, (2) diffusion of the solutes from the contacts into the pore spaces, (3) precipitation on interfaces with low stress, including the pore walls, with the assumption that these processes are steady state mass transport controlled, with the lowest rate controlling the overall rate of deformation.

So within all these approaches, the activation energies and diffusional pathways are of importance, which is the target of this paper, but in future studies, the kinetics have to also be considered with the details of the other parameters, such as particle size, material type, crystal anisotropy, and surface speciation, to mention but a few. It is clear that we have to ultimately consider all these interplaying parameters, within a self-consistent model.

Nevertheless, the complexity of other potential mechanisms, such as precipitation reaction or diffusion of solutes into the solvent of the pore space, opens perspectives towards a more complete investigation of the whole densification process with various applied pressures and material / solvent couples. To do so, other variables could be integrated, such as a porosity function or a pressure factor, or grain size, in order to get a broader look at the complete picture that will allow the study of the sintering mechanisms involved in low temperature sintering processes.

Acknowledgements:

This work has been made possible by the financial support of the French National Research Agency (ANR) in the framework of the project HYDILIC (ANR-18-CE08-0006), and Arnaud Ndayishimiye and Clive A. Randall are thankful for coverage from the AFOSR (FA9550-19-1-0372) that contributed their efforts to this article

References

[1] R.L. Coble, Initial Sintering of Alumina and Hematite, J. Am. Ceram. Soc. 41 (1958) 55–62. https://doi.org/10.1111/j.1151-2916.1958.tb13519.x.

[2] W.D. Kingery, Densification during Sintering in the Presence of a Liquid Phase. I. Theory, J. Appl. Phys. 30 (1959) 301–306. https://doi.org/10.1063/1.1735155.

[3] M.G. Randall, Sintering: from Empirical Observations to Scientific Principles, Butterworth-Heinemann, 2014. https://doi.org/10.1016/C2012-0-00717-X.

[4] M.N. Rahaman, Sintering of Ceramics, 1st Edition, CRC Press, Boca Raton, 2007. https://doi.org/10.1201/b15869.

[5] M. Biesuz, S. Grasso, V.M. Sglavo, What's new in ceramics sintering? A short report on the latest trends and future prospects, Curr. Opin. Solid State Mater. Sci. 24 (2020) 100868. https://doi.org/10.1016/j.cossms.2020.100868.

[6] M. Cologna, B. Rashkova, R. Raj, Flash Sintering of Nanograin Zirconia in <5 s at 850°C: Rapid Communications of the American Ceramic Society, J. Am. Ceram. Soc. 93 (2010) 3556–3559. https://doi.org/10.1111/j.1551-2916.2010.04089.x.

[7] M. Biesuz, V.M. Sglavo, Flash sintering of ceramics, J. Eur. Ceram. Soc. 39 (2019) 115–143. https://doi.org/10.1016/j.jeurceramsoc.2018.08.048.

[8] M. Yu, S. Grasso, R. Mckinnon, T. Saunders, M.J. Reece, Review of flash sintering: materials, mechanisms and modelling, Adv. Appl. Ceram. 116 (2017) 24–60. https://doi.org/10.1080/17436753.2016.1251051.

[9] M.Z. Becker, N. Shomrat, Y. Tsur, Recent Advances in Mechanism Research and Methods for Electric-Field-Assisted Sintering of Ceramics, Adv. Mater. 30 (2018) 1706369. https://doi.org/10.1002/adma.201706369.

[10] O. Guillon, J. Gonzalez-Julian, B. Dargatz, T. Kessel, G. Schierning, J. Räthel, M. Herrmann, Field-Assisted Sintering Technology/Spark Plasma Sintering: Mechanisms, Materials, and Technology Developments, Adv. Eng. Mater. 16 (2014) 830–849. https://doi.org/10.1002/adem.201300409.

[11] G. Cao, C. Estournès, J.E. Garay, Spark plasma sintering : current status, new developments and challenges a review of the current trends in SPS, Amsterdam : Elsevier, Amsterdam (Pays-Bas), 2019.

[12] G. Bernard-Granger, C. Guizard, Spark plasma sintering of a commercially available granulated zirconia powder: I. Sintering path and hypotheses about the mechanism(s) controlling densification, Acta Mater. 55 (2007) 3493–3504. https://doi.org/10.1016/j.actamat.2007.01.048.

[13] E.A. Olevsky, L. Froyen, Impact of Thermal Diffusion on Densification During SPS, J. Am. Ceram. Soc. 92 (2009) S122–S132. https://doi.org/10.1111/j.1551-2916.2008.02705.x.

[14] R. Castro, K. van Benthem, eds., Sintering: Mechanisms of Convention Nanodensification and Field Assisted Processes, Springer Berlin Heidelberg, Berlin, Heidelberg, 2013. https://doi.org/10.1007/978-3-642-31009-6.

[15] M. Biesuz, D. Rizzi, V.M. Sglavo, Electric current effect during the early stages of field-assisted sintering, J. Am. Ceram. Soc. (2018). https://doi.org/10.1111/jace.15976.

[16] R. Chaim, G. Chevallier, A. Weibel, C. Estournès, Grain growth during spark plasma and flash sintering of ceramic nanoparticles: a review, J. Mater. Sci. 53 (2018) 3087–3105. https://doi.org/10.1007/s10853-017-1761-7.

[17] W.D. Kingery, M. Berg, Study of the Initial Stages of Sintering Solids by Viscous Flow, Evaporation-Condensation, and Self-Diffusion, J. Appl. Phys. 26 (1955) 1205–1212. https://doi.org/10.1063/1.1721874.

[18] W.D. Kingery, J.M. Woulbroun, F.R. Charvat, Effects of Applied Pressure on Densification During Sintering in the Presence of a Liquid Phase, J. Am. Ceram. Soc. 46 (1963) 391–395. https://doi.org/10.1111/j.1151-2916.1963.tb11758.x.

[19] J.E. Burke, Role of Grain Boundaries in Sintering., J. Am. Ceram. Soc. 40 (1957) 80–85. https://doi.org/10.1111/j.1151-2916.1957.tb12580.x.

[20] D.L. Johnson, I.B. Cutler, Diffusion Sintering: I, Initial Stage Sintering Models and Their Application to Shrinkage of Powder Compacts, J. Am. Ceram. Soc. 46 (1963) 541–545. https://doi.org/10.1111/j.1151-2916.1963.tb14606.x.

[21] D.L. Johnson, New Method of Obtaining Volume, Grain-Boundary, and Surface Diffusion Coefficients from Sintering Data, J. Appl. Phys. 40 (1969) 192–200. https://doi.org/10.1063/1.1657030.

[22] R.L. Coble, Sintering Crystalline Solids. I. Intermediate and Final State Diffusion Models, J. Appl. Phys. 32 (1961) 787–792. https://doi.org/10.1063/1.1736107.

[23] J.L. Woolfrey, M.J. Bannister, Nonisothermal Techniques for Studying Initial-Stage Sintering, J. Am. Ceram. Soc. 55 (1972) 390–394. https://doi.org/10.1111/j.1151-2916.1972.tb11319.x.

[24] H. Su, D.L. Johnson, Master Sintering Curve: A Practical Approach to Sintering, J. Am. Ceram. Soc. 79 (1996) 3211–3217. https://doi.org/10.1111/j.1151-2916.1996.tb08097.x.

[25] M.F. Ashby, A first report on sintering diagrams, Acta Metall. 22 (1974) 275–289. https://doi.org/10.1016/0001-6160(74)90167-9.

[26] M.L. Huckabee, T.M. Hare, H. Palmour, Rate Controlled Sintering as a Processing Method, in: H. Palmour, R.F. Davis, T.M. Hare (Eds.), Process. Cryst. Ceram., Springer US, Boston, MA, 1978: pp. 205–215. https://doi.org/10.1007/978-1-4684-3378-4_18.

[27] W.S. Young, I.B. Cutler, Initial Sintering with Constant Rates of Heating, J. Am. Ceram. Soc. 53 (1970) 659–663. https://doi.org/10.1111/j.1151-2916.1970.tb12036.x.

[28] S.H. Hillman, R.M. German, Constant heating rate analysis of simultaneous sintering mechanisms in alumina, J. Mater. Sci. 27 (1992) 2641–2648. https://doi.org/10.1007/BF00540683.

[29] K. Matsui, N. Ohmichi, M. Ohgai, N. Enomoto, J. Hojo, Sintering Kinetics at Constant Rates of Heating: Effect of Al2O3 on the Initial Sintering Stage of Fine Zirconia Powder, J. Am. Ceram. Soc. 88 (2005) 3346–3352. https://doi.org/10.1111/j.1551-2916.2005.00620.x.

[30] A. Ndayishimiye, M.Y. Sengul, T. Sada, S. Dursun, S.H. Bang, Z.A. Grady, K. Tsuji, S. Funahashi, A.C.T. van Duin, C.A. Randall, Roadmap for densification in cold sintering: Chemical pathways, Open Ceram. (2020) 100019. https://doi.org/10.1016/j.oceram.2020.100019.

[31] J. Guo, R. Floyd, S. Lowum, J.-P. Maria, T. Herisson de Beauvoir, J.-H. Seo, C.A. Randall, Cold Sintering: Progress, Challenges, and Future Opportunities, Annu. Rev. Mater. Res. 49 (2019) 275–295. https://doi.org/10.1146/annurev-matsci-070218-010041.

[32] J.-P. Maria, X. Kang, R.D. Floyd, E.C. Dickey, H. Guo, J. Guo, A. Baker, S. Funihashi, C.A. Randall, Cold sintering: Current status and prospects, J. Mater. Res. 32 (2017) 3205–3218. https://doi.org/10.1557/jmr.2017.262.

[33] N. Yamasaki, K. Yanagisawa, M. Nishioka, S. Kanahara, A hydrothermal hot-pressing method: Apparatus and application, J. Mater. Sci. Lett. 5 (1986) 355–356.

[34] G. Goglio, A. Largeteau, A. Ndayishimiye, M. Prakasam, Procédé et dispositif de densification de matériaux ou de consolidation d’un assemblage de matériaux par frittage hydrothermal ou solvothermal, FR17/54585, 2017.

[35] G. Goglio, A. Ndayishimiye, A. Largeteau, C. Elissalde, View point on hydrothermal sintering: Main features, today’s recent advances and tomorrow’s promises, Scr. Mater. 158 (2019) 146–152. https://doi.org/10.1016/j.scriptamat.2018.08.038.

[36] A. Ndayishimiye, A. Largeteau, S. Mornet, M. Duttine, M.-A. Dourges, D. Denux, M. Verdier, M. Gouné, T. Hérisson de Beauvoir, C. Elissalde, G. Goglio, Hydrothermal Sintering for Densification of Silica. Evidence for the Role of Water, J. Eur. Ceram. Soc. 38 (2018) 1860–1870. https://doi.org/10.1016/j.jeurceramsoc.2017.10.011.

[37] A. Ndayishimiye, A. Largeteau, M. Prakasam, S. Pechev, M.-A. Dourges, G. Goglio, Low temperature hydrothermal sintering process for the quasi-complete densification of nanometric α-quartz, Scr. Mater. 145 (2018) 118–121. https://doi.org/10.1016/j.scriptamat.2017.10.023.

[38] A. Ndayishimiye, M.Y. Sengul, S.H. Bang, K. Tsuji, K. Takashima, T. Hérisson de Beauvoir, D. Denux, J.-M. Thibaud, A.C.T. van Duin, C. Elissalde, G. Goglio, C.A. Randall, Comparing hydrothermal sintering and cold sintering process: Mechanisms, microstructure, kinetics and chemistry, J. Eur. Ceram. Soc. 40 (2020) 1312–1324. https://doi.org/10.1016/j.jeurceramsoc.2019.11.049.

[39] J. Gonzalez-Julian, K. Neuhaus, M. Bernemann, J. Pereira da Silva, A. Laptev, M. Bram, O. Guillon, Unveiling the mechanisms of cold sintering of ZnO at 250 °C by varying applied stress and characterizing grain boundaries by Kelvin Probe Force Microscopy, Acta Mater. 144 (2018) 116–128. https://doi.org/10.1016/j.actamat.2017.10.055.

[40] S.H. Bang, A. Ndayishimiye, C.A. Randall, Anisothermal densification kinetics of the cold sintering process below 150 °C, J. Mater. Chem. C. 8 (2020) 5668–5672. https://doi.org/10.1039/D0TC00395F.

[41] T.K. Roy, A. Ghosh, Sintering and grain growth kinetics in undoped and silica doped zinc oxide ceramics, Ceram. Int. 40 (2014) 10755–10766. https://doi.org/10.1016/j.ceramint.2014.03.065.

[42] K.G. Ewsuk, D.T. Ellerby, C.B. DiAntonio, Analysis of Nanocrystalline and Microcrystalline ZnO Sintering Using Master Sintering Curves, J. Am. Ceram. Soc. 89 (2006) 2003–2009. https://doi.org/10.1111/j.1551-2916.2006.00990.x.

[43] S.-J.L. Kang, Sintering: Densification, grain growth and microstructure, Elsevier Butterworth-Heinemann, Amsterdam Boston London, 2005.

[44] D. Bernache-Assollant, Chimie-physique du frittage, Paris : Hermès, Paris (France), 1993.

[45] R.L. Coble, Diffusion Models for Hot Pressing with Surface Energy and Pressure Effects as Driving Forces, J. Appl. Phys. 41 (1970) 4798–4807. https://doi.org/10.1063/1.1658543.

[46] S. Bordère, J.-P. Caltagirone, A multi-physics and multi-time scale approach for modeling fluid–solid interaction and heat transfer, Comput. Struct. 164 (2016) 38–52. https://doi.org/10.1016/j.compstruc.2015.10.009.

[47] G. Taveri, S. Grasso, F. Gucci, J. Toušek, I. Dlouhy, Bio-Inspired Hydro-Pressure Consolidation of Silica, Adv. Funct. Mater. 28 (2018) 1805794. https://doi.org/10.1002/adfm.201805794.

[48] M.P.A. van den Ende, G. Marketos, A.R. Niemeijer, C.J. Spiers, Investigating Compaction by Intergranular Pressure Solution Using the Discrete Element Method, J. Geophys. Res. Solid Earth. 123 (2018) 107–124. https://doi.org/10.1002/2017JB014440.

[49] J.-P. Gratier, D.K. Dysthe, F. Renard, The Role of Pressure Solution Creep in the Ductility of the Earth's Upper Crust, in: Adv. Geophys., Elsevier, 2013: pp. 47–179. https://doi.org/10.1016/B978-0-12-380940-7.00002-0.

[50] S. de Meer, C.J. Spiers, Uniaxial compaction creep of wet gypsum aggregates, J. Geophys. Res. Solid Earth. 102 (1997) 875–891. https://doi.org/10.1029/96JB02481.

[51] A.R. Niemeijer, C.J. Spiers, B. Bos, Compaction creep of quartz sand at 400–600°C: experimental evidence for dissolution-controlled pressure solution, Earth Planet. Sci. Lett. 195 (2002) 261–275. https://doi.org/10.1016/S0012-821X(01)00593-3.

[52] C.J. Spiers, S. De Meer, A.R. Niemeijer, X. Zhang, Kinetics of rock deformation by pressure solution and the role of the thin aqueous films, in: Physicochem. Water Geol. Biol. Syst., S. Nakasimha, C. J. Spiers, L. Mercury, P. A. Fenter, M. F. J Hochella, Tokyo, Japan, 2004: pp. 129–158.

[53] M.S. Paterson, Nonhydrostatic thermodynamics and its geologic applications, Rev. Geophys. 11 (1973) 355. https://doi.org/10.1029/RG011i002p00355.

[54] R.B. De Boer, On the thermodynamics of pressure solution—interaction between chemical and mechanical forces, Geochim. Cosmochim. Acta. 41 (1977) 249–256. https://doi.org/10.1016/0016-7037(77)90232-0.

[55] B. Malvoisin, L.P. Baumgartner, Mineral Dissolution and Precipitation Under Stress: Model Formulation and Application to Metamorphic Reactions, Geochem. Geophys. Geosystems. 22 (2021). https://doi.org/10.1029/2021GC009633.
[56] M. Biesuz, G. Taveri, A.I. Duff, E. Olevsky, D. Zhu, C. Hu, S. Grasso, A theoretical analysis of cold sintering, Adv. Appl. Ceram. 119 (2020) 75–89. https://doi.org/10.1080/17436753.2019.1692173.
[57] S.J. Glass, K.G. Ewsuk, Ceramic Powder Compaction, MRS Bull. 22 (1997) 24–28. https://doi.org/10.1557/S0883769400034709.
[58] W.M. Long, Radial pressures in powder compaction, Powder Metall. 3 (1960) 73–86. https://doi.org/10.1179/pom.1960.3.6.005.
[59] L. Viers, F. Delaunay, R. Boulesteix, M. Vandenhende, G. Antou, A. Maître, Study of densification mechanisms during Spark Plasma Sintering of co-precipitated Ho:Lu2O3 nanopowders: Application to transparent ceramics for lasers, J. Eur. Ceram. Soc. 41 (2021) 7199–7207. https://doi.org/10.1016/j.jeurceramsoc.2021.07.028.
[60] C. Liu, A. Wang, T. Tian, L. Hu, W. Guo, Q. He, J. Xie, W. Wang, H. Wang, Z. Fu, Sintering and densification mechanisms of tantalum carbide ceramics, J. Eur. Ceram. Soc. 41 (2021) 7469–7477. https://doi.org/10.1016/j.jeurceramsoc.2021.07.047.
[61] R.L. Coble, J.S. Ellis, Hot-Pressing Alumina-Mechanisms of Material Transport, J. Am. Ceram. Soc. 46 (1963) 438–441. https://doi.org/10.1111/j.1151-2916.1963.tb11771.x.
[62] H.F. Fischmeister, E. Arzt, L.R. Olsson, Particle Deformation and Sliding During Compaction of Spherical Powders: A Study by Quantitative Metallography, Powder Metall. 21 (1978) 179–187. https://doi.org/10.1179/pom.1978.21.4.179.
[63] A.S. Helle, K.E. Easterling, M.F. Ashby, Hot-isostatic pressing diagrams: New developments, Acta Metall. 33 (1985) 2163–2174. https://doi.org/10.1016/0001-6160(85)90177-4.
[64] J. Langer, M.J. Hoffmann, O. Guillon, Electric Field-Assisted Sintering and Hot Pressing of Semiconductive Zinc Oxide: A Comparative Study: Fast Sintering and Hot Pressing of Semiconductive Zinc Oxide, J. Am. Ceram. Soc. 94 (2011) 2344–2353. https://doi.org/10.1111/j.1551-2916.2011.04396.x.
[65] N. Louet, H. Reveron, G. Fantozzi, Sintering behaviour and microstructural evolution of ultrapure α-alumina containing low amounts of SiO2, J. Eur. Ceram. Soc. 28 (2008) 205–215. https://doi.org/10.1016/j.jeurceramsoc.2007.04.015.
[66] J.E. Dorn, The spectrum of activation energies for creep, in: R. Maddin, Cleveland, Ohio, 1957: pp. 255–283.
[67] J.J. Bacmann, G. Cizeron, Dorn Method in the Study of Initial Phase of Uranium Dioxide Sintering, J. Am. Ceram. Soc. 51 (1968) 209–212. https://doi.org/10.1111/j.1151-2916.1968.tb11874.x.
[68] F. Paulik, J. Paulik, Investigations under quasi-isothermal and quasi-isobaric conditions by means of the Derivatograph, J. Therm. Anal. 5 (1973) 253–270. https://doi.org/10.1007/BF01950373.
[69] J. Rouquerol, Critical examination of several problems typically found in the kinetic study of thermal decomposition under vacuum, J. Therm. Anal. 5 (1973) 203–216. https://doi.org/10.1007/BF01950369.
[70] S. Bordère, F. Rouquerol, J. Rouquerol, J. Estienne, A. Floreancig, Kinetical possibilities of controlled transformation Rate Thermal Analysis (CRTA): Application to the thermolysis of hexahydrated uranyl nitrate, J. Therm. Anal. 36 (1990) 1651–1668. https://doi.org/10.1007/BF01913412.
[71] O.T. SØrensen, Thermogravimetric and dilatometric studies using Stepwise Isothermal Analysis and related techniques, J. Therm. Anal. 38 (1992) 213–228. https://doi.org/10.1007/BF02109120.

[72] S. Funahashi, J. Guo, H. Guo, K. Wang, A.L. Baker, K. Shiratsuyu, C.A. Randall, Demonstration of the cold sintering process study for the densification and grain growth of ZnO ceramics, J. Am. Ceram. Soc. 100 (2017) 546–553. https://doi.org/10.1111/jace.14617.

[73] T.K. Gupta, R.L. Coble, Sintering of ZnO: I, Densification and Grain Growth*, J. Am. Ceram. Soc. 51 (1968) 521–525. https://doi.org/10.1111/j.1151-2916.1968.tb15679.x.

[74] B. Dargatz, J. Gonzalez-Julian, M. Bram, P. Jakes, A. Besmehn, L. Schade, R. Röder, C. Ronning, O. Guillon, FAST/SPS sintering of nanocrystalline zinc oxide—Part I: Enhanced densification and formation of hydrogen-related defects in presence of adsorbed water, J. Eur. Ceram. Soc. 36 (2016) 1207–1220. https://doi.org/10.1016/j.jeurceramsoc.2015.12.009.

[75] N. Neves, R. Barros, E. Antunes, I. Ferreira, J. Calado, E. Fortunato, R. Martins, Sintering Behavior of Nano- and Micro-Sized ZnO Powder Targets for rf Magnetron Sputtering Applications, J. Am. Ceram. Soc. 95 (2012) 204–210. https://doi.org/10.1111/j.1551-2916.2011.04874.x.

[76] J. Han, A.M.R. Senos, P.Q. Mantas, Nonisothermal sintering of Mn doped ZnO, J. Eur. Ceram. Soc. 19 (1999) 1003–1006. https://doi.org/10.1016/S0955-2219(98)00362-8.

[77] F.K. Crundwell, The mechanism of dissolution of minerals in acidic and alkaline solutions: Part III. Application to oxide, hydroxide and sulfide minerals, Hydrometallurgy. 149 (2014) 71–81. https://doi.org/10.1016/j.hydromet.2014.06.008.

[78] L. JORET, Influence d’un rayonnement microonde sur la cinetique de dissolution de uo2, ceo2 et co3o4 en milieu nitrique, 1995.

[79] B. Terry, Specific chemical rate constants for the acid dissolution of oxides and silicates, Hydrometallurgy. 11 (1983) 315–344. https://doi.org/10.1016/0304-386X(83)90051-8.

[80] V.V. Danilov, N.M. Sorokin, A.A. Ravdel, Dissolution of zinc oxide in aqueous solutions of perchloric, hydrochloric, and acetic acids, Zhurnal Prikl. Khimii. 49 (1976) 1006–1010.

[81] D. Cardoso, A. Narcy, S. Durosoy, C. Bordes, Y. Chevalier, Dissolution kinetics of zinc oxide and its relationship with physicochemical characteristics, Powder Technol. 378 (2021) 746–759. https://doi.org/10.1016/j.powtec.2020.10.049.

[82] J.T. Hughes, A. Navrotsky, Enthalpy of formation of zinc acetate dihydrate, J. Chem. Thermodyn. 43 (2011) 980–982. https://doi.org/10.1016/j.jct.2011.02.004.

[83] M.Y. Sengul, J. Guo, C.A. Randall, A.C.T. van Duin, Water-Mediated Surface Diffusion Mechanism Enables the Cold Sintering Process: A Combined Computational and Experimental Study, Angew. Chem. Int. Ed. 58 (2019) 12420–12424. https://doi.org/10.1002/anie.201904738.

[84] A. Moezzi, A. McDonagh, A. Dowd, M. Cortie, Zinc Hydroxyacetate and Its Transformation to Nanocrystalline Zinc Oxide, Inorg. Chem. 52 (2013) 95–102. https://doi.org/10.1021/ic302328e.

[85] H. Gerischer, N. Sorg, Chemical dissolution of zinc oxide crystals in aqueous electrolytes—An analysis of the kinetics, Electrochimica Acta. 37 (1992) 827–835. https://doi.org/10.1016/0013-4686(92)85035-J.

[86] E.A. Meulenkamp, Size Dependence of the Dissolution of ZnO Nanoparticles, J. Phys. Chem. B. 102 (1998) 7764–7769. https://doi.org/10.1021/jp982305u.

[87] M. Hurşit, O. Laçin, H. Saraç, Dissolution kinetics of smithsonite ore as an alternative zinc source with an organic leach reagent, J. Taiwan Inst. Chem. Eng. 40 (2009) 6–12. https://doi.org/10.1016/j.jtice.2008.07.003.

[88] A. Zeumault, S.K. Volkman, Probing the Kinetics of Crystallite Growth in Sol–Gel Derived Metal-Oxides Using Nanocalorimetry, Cryst. Growth Des. 20 (2020) 1590–1597. https://doi.org/10.1021/acs.cgd.9b01339.

[89] Z. Liu, C. Zhou, B. Li, L. Zhang, Y. Liang, Effects of grain dissolution–diffusion sliding and hydro-mechanical interaction on the creep deformation of soft rocks, Acta Geotech. 15 (2020) 1219–1229. https://doi.org/10.1007/s11440-019-00823-9.

[90] R. Raj, Creep in polycrystalline aggregates by matter transport through a liquid phase, J. Geophys. Res. Solid Earth. 87 (1982) 4731–4739. https://doi.org/10.1029/JB087iB06p04731.

[91] E.H. Rutter, Pressure solution in nature, theory and experiment, J. Geol. Soc. 140 (1983) 725–740. https://doi.org/10.1144/gsjgs.140.5.0725.

[92] F.K. Lehner, Thermodynamics of rock deformation by pressure solution, in: D.J. Barber, P.G. Meredith (Eds.), Deform. Process. Miner. Ceram. Rocks, Springer Netherlands, Dordrecht, 1990: pp. 296–333. https://doi.org/10.1007/978-94-011-6827-4_12.

[93] C.J. Spiers, P.M.T.M. Schutjens, R.H. Brzesowsky, C.J. Peach, J.L. Liezenberg, H.J. Zwart, Experimental determination of constitutive parameters governing creep of rocksalt by pressure solution, Geol. Soc. Lond. Spec. Publ. 54 (1990) 215–227. https://doi.org/10.1144/GSL.SP.1990.054.01.21.

[94] X. Zhang, C.J. Spiers, Compaction of granular calcite by pressure solution at room temperature and effects of pore fluid chemistry, Int. J. Rock Mech. Min. Sci. 42 (2005) 950–960. https://doi.org/10.1016/j.ijrmms.2005.05.017.

[95] S.D. Meer, C.J. Spiers, C.J. Peach, Kinetics of precipitation of gypsum and implications for pressure-solution creep, J. Geol. Soc. 157 (2000) 269–281. https://doi.org/10.1144/jgs.157.2.269.

[96] X. Zhang, C.J. Spiers, C.J. Peach, Compaction creep of wet granular calcite by pressure solution at 28°C to 150°C, J. Geophys. Res. 115 (2010) B09217. https://doi.org/10.1029/2008JB005853.